1-1-2013

Synthesis and Characterization of New Ionic and Mixed Ionic/Electronic Conductors

Kevin Gregory Romito
University of South Carolina

Recommended Citation

Romito, K. G.(2013). *Synthesis and Characterization of New Ionic and Mixed Ionic/Electronic Conductors.* (Master's thesis). Retrieved from https://scholarcommons.sc.edu/etd/2334

SYNTHESIS AND CHARACTERIZATION
OF
NEW IONIC AND MIXED IONIC/ELECTRONIC CONDUCTORS

By

Kevin Gregory Romito

Bachelor of Science
University of South Carolina, 2011

Submitted on Partial Fulfillment of the Requirements

For the Degree of Master of Science in

Mechanical Engineering

College of Engineering and Computing

University of South Carolina

2013

Accepted by:

Kevin Huang, Major Professor

Xingjian Xue, Committee Member

Lacy Ford, Vice Provost and Dean of Graduate Studies

ABSTRACT

In a constantly growing and developing world, there is a great need to develop new forms of clean energy generation. Many solutions have been proposed to ameliorate these global concerns, which include fuel cell technology and new processes for reducing polluting chemicals in the atmosphere. These technologies are still in their infancy and require further development before becoming viable options.

In the case of fuel cells, particularly solid oxide fuel cells, and CO_2 separation membranes, there is a need to develop ion conducting materials that are highly efficient, less costly to synthesize, and can perform strongly under many real-world conditions. The need for further developing these ion conductors is currently one of the most important final steps required to push these new technologies into the market. The research presented here focuses on the synthesis and characterization for several ion conductor systems intended for efficient energy conversion applications.

Using a novel transient liquid phase sintering method, we demonstrate that it is possible to synthesize dense $BaZr_{0.8}Y_{0.2}O_{3-\delta}$ (BZY20) at 1300°C, a lower temperature than previously reported, using barium gallate as a sintering flux.

Focusing on a new family of oxide-ion conductors, $Sr_{1-x}K_xSi_{1-y}Ge_yO_{3-0.5x}$, gallium served as a replacement germanium in an effort to further increase the oxide-ion conductivity. Unfortunately, the replacement of Ge with Ga was found to decrease the overall oxide-ion conductivity and microstructural morphology.

Through the addition of an Al_2O_3 layer to a porous silver matrix, we show that CO_2 permeation flux density through a new MECC membrane can be enhanced as a result of improved retention of molten carbonate in the silver matrix. Pore size and distribution in the silver matrix were found to greatly depend on the concentration of Al_2O_3 suspension.

TABLE OF CONTENTS

CHAPTER 1: INTRODUCTION

CHAPTER 2: NOVEL METHOD FOR DENSIFYING PROTON CONDUCTORS

CHAPTER 3: POTENTIAL ADVANCEMENT FOR NEW OXIDE-ION CONDUCTOR

CHAPTER 4: NEW DEVELOPMENTS IN MECC SYNTHESIS

List of Figures

CHAPTER 1:

INTRODUCTION

1.1 Background

In recent years, there has been an increasing interest in new forms of alternative energy. Both industry and society have deemed fossil fuel based energy to be outdated and detrimental to the environment. Currently mass produced technology based on fossil fuels negatively impacts our environment due to the release of greenhouse gases and hydrocarbon emissions, which contribute to global warming. Similarly, the majority of the developed world still bases their energy production on the burning of coal, which also releases toxic gases and greenhouse gases into the atmosphere. In the past, there has been little regulation for these byproducts and the effects of global warming appear to be increasing exponentially as a result.

Aside from the pollution caused to the environment, there are still many developing countries that suffer from a lack of energy resources, partially due to the scarcity and high cost of fossil fuels. It is unlikely that these sources of energy will be effectual in aiding developing countries.

It is well known that energy is the most important asset for stimulating human progress. From a short term perspective, there is a large amount of research invested in the removal of harmful emissions from fossil fuel based power plants. In terms of long term research, engineers and scientists now look towards the future to develop highly efficient, inexpensive, and eco-friendly forms of energy conversion and storage technology.

One promising form of energy conversion is the fuel cell. Fuel cells are by no means a new technology; however, there have been recent developments in polymeric and ceramic materials that make fuel cells an attractive alternative to the fossil fuel based technology, such as the internal combustion engine. Automobiles based on the combustion engine have an overall efficiency of 20-30% [1]. When closely observing these low efficiencies, there is a noticeable amount of thermal energy wasted; therefore, the costly fossil fuels used for energy conversion are being wasted as well. Fuel cells, on the other hand, have the capability of reaching their high theoretical efficiencies more closely than combustion engines because of the direct conversion from chemical energy to electrical energy.

1.2 Solid Oxide Fuel Cells

Fuel cells are electrochemical cells made up of three major components: a cathode, an anode, and an electrolyte. The basic structure of a cell consists of an electrolyte with the electrodes (cathode and anode) at the electrolyte interfaces. Fuel, generally hydrogen, is delivered to the anode side of the fuel cell, while the cathode is exposed to an oxygen source. The hydrogen fuel goes through a series of electrochemical reactions, generating electricity between the electrodes. Fuel cell types differ due to the electrolyte and electrode materials utilized in the cell, which in turn governs the type electrochemical reactions that take place to convert chemical energy to electrical energy. The working mechanism for solid oxide fuel cell technology can be seen in Figure 1.1. Oxygen-ion electrolytes usually include doped zirconia, doped ceria, doped bismuth oxide, and doped lanthanum gallate [1]. SOFC anodes usually utilize electrolyte materials mixed with nickel, while cathodes are comprised of electronically conductive or mixed conducting materials, such as doped lanthanum strontium manganites and lanthanum strontium ferrites.

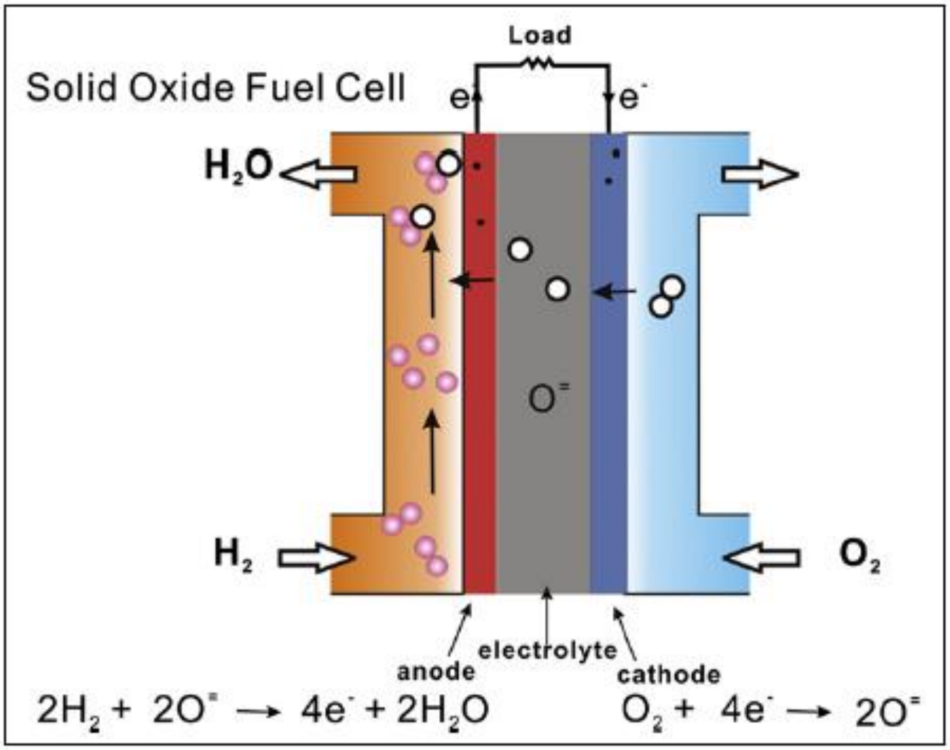

Figure 1.1 SOFC working principle [2].

A major contender amongst fuel cell types, the solid oxide fuel cell (SOFC) has many benefits aside from the advantages generally associated with fuel cells. All fuel cells are known to be highly efficient, capable of providing continuous energy production, and produce little to no harmful emissions; along with these advantages, SOFCs tend to have chemically stable electrolytes and these fuel cells may utilize a variety of different fuels. Despite these benefits, SOFCs still have imperfections that must be overcome in order to become a viable source of power generation. A major drawback is the high temperatures required for operating these cells. For many years, oxide-ion conducting materials were primarily researched as electrolytes for SOFCs; however, when trying to reduce the operating temperature of the cells, electrode polarization resistances and electrolyte resistance tend to increase [1]. One way to decrease the electrolyte resistance is by creating thinner electrolytes to ultimately decrease the ohmic losses over the cell. Another possibility for decreasing this resistance is to find alternative electrolyte materials with better conductivity at lower operating temperatures. The other major problem with SOFCs is the increasing electrode over-potentials as operating temperatures decrease. These increasing over-potentials are often associated with the rate-limiting reactions of the cathode materials. The kinetics of the oxygen-reduction reactions occurring at the cathode are much slower than the kinetics of the hydrogen-oxidation reactions of the anode, thus oxygen-reduction bottle-necks the overall reaction speed [1].

For cells based on oxide-ion conducting electrolytes, O^{2-} ions migrate from the air introduced at the cathode of the cell, to the anode. The fuel introduced at the anode, using hydrogen as an example, reacts with the oxygen-ion to release electron to the load and produce exhaust, water. The most commonly studied and used oxygen-ion electrolyte is yttria-stabilized zirconia (YSZ). Through defect chemistry, it is known that YSZ contains oxygen vacancies, enabling the high oxygen-ion conductivity [1].

1.3 High Temperature Proton Conductors

The consideration of new electrolyte materials has led researchers to the option of high temperature proton conductors (HTPCs) as an alternative to the oxide-ion conducting electrolytes commonly associated with SOFCs. HTPCs are considered a promising alternative due to larger conductivities in the intermediate temperature range. For HTPC based cells, the hydrogen fuel reacts with the anode, converting the fuel into protons that migrate throughout the HTPC electrolyte due to point defects in the lattice. Based on the Grotthuss-type mechanism, the migrating protons form weak hydrogen bonds with the oxides in the lattice, which are promptly cleaved and the protons continue this process, migrating towards the electrolyte/cathode interface, this process is visualized in Figure 1.2 [1]. At the electrolyte/cathode interface, the migrating protons react with oxygen, creating water as a byproduct. The Grotthuss-type mechanism utilized by HTPCs, transports the protons at a much lower activation energy than the energy required for oxygen-ion transport. Overall, the low activation energy leads to higher conductivity at intermediate temperatures (IT).

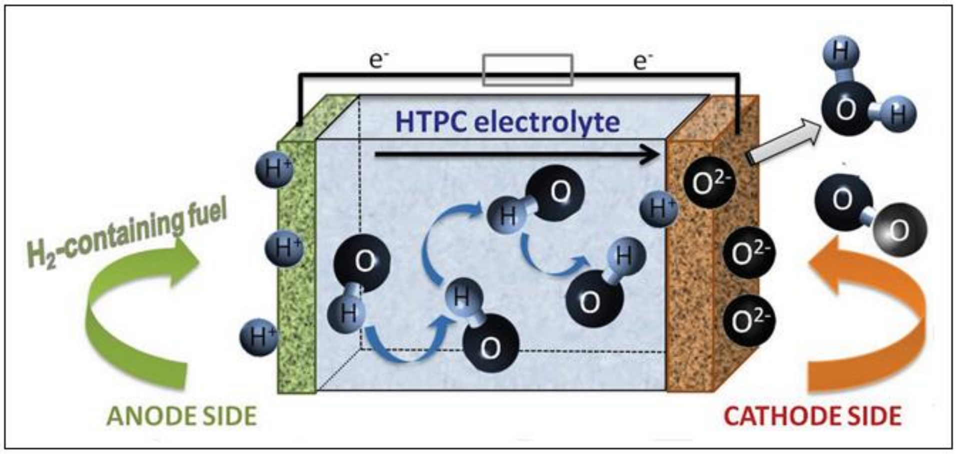

Figure 1.2 SOFC based on high temperature proton conductors with protons migrating through Grotthuss-type mechanism [1].

Fuel cell performance is strongly influenced by the properties of an electrolyte. To aid reduction of ohmic losses, electrolyte layers of a cell must be optimally thin. However, if the electrolyte is too thin, it may negatively affect mechanical durability and the grain structure of the material. Electrolytes may contribute a maximum of $0.15\Omega\text{cm}^2$ to the total cell resistance, while still maintaining a reasonable conductivity at operating temperatures [3]. To maximize the open circuit voltage, the electrolyte must be dense to prevent gas leakage through the electrolyte and to prevent direct interactions between the two electrodes. The electrolyte must be chemically stable to withstand oxidizing and reducing environments and in atmospheres containing high levels of steam and carbon dioxide.

1.4 Perovskite Structured Proton Conductors

The predominant material structure utilized for high temperature proton conductors are of the perovskite structure (ABO_3). Perovskites tend to show exceptional proton conductivity, specifically materials based on yittria-doped barium zirconate (BZY), in the IT range (350°C - 600°C) and wet atmospheres [1]. When utilizing acceptor doping at the B site of perovskites, containing an octahedral coordination, oxygen vacancies are created within the lattice. Through the incorporation of water into the vacancies, proton conduction is stimulated through the following defect reaction.

$$H_2O_{(g)} + V_{\ddot{O}} + O_O^x = 2OH_{\dot{O}} \qquad (1.1)$$

Problems present in these materials are poor sinterability and poor chemical stability. To help cope with the sinterability issue, two methods have been proposed: sintering aids and wet chemical synthesis.

In early studies on HTPCs, acceptor-doped barium cerates, specifically yttria-doped barium cerate (BCY), displayed the some of the highest proton conductivity. However, BCY is hindered by its reactivity with acidic gases, primarily CO_2 and SO_2, and water vapor, which are present under operating conditions [5, 6]. Due to these shortcomings, yttrium-doped barium zirconate (BZY) has been the subject of numerous studies.

BZY electrolytes are considered more promising than BCY electrolytes due to its chemical stability when introduced to acidic atmospheres. BZY also displays good proton conductivity and requires smaller activation energy when compared to other electrolyte materials [4]. Further development is required to make BZY a viable option as a marketable SOFC electrolyte material. The poor sinterability of BZY is the challenge to material's major applications [4]. Other issues include poor conductivity at the grain boundaries.

Barium zirconate doped with 20 mol% yttria (BZY20), $BaZr_{0.8}Y_{0.2}O_{3-\delta}$ is considered one of the most promising proton conducting electrolyte materials. BZY20 has displayed the lowest activation energy and largest proton conductivity in the BZY family. When tested under wet conditions at intermediate temperatures (400°C - 700°C), BZY20 is nearly a pure proton conductor with negligible electronic conductivity [1]. As with any other BZY material, BZY20 suffers from poor sinterability.

Extensive lists of sintering aids have been tested with BZY in an attempt to lower the densification temperature and to promote favorable grain growth during densification. Mixing small percentages of different oxides with pre-sintered BZY may theoretically promote good sinterability, but these sintering aids either hindered proton conductivity or introduced electronic conductivity [7, 8].

Wet synthesis methods allow for sintering temperatures to be lowered due to a its ability to make nanoscale powders [1]. This wet chemical synthesis, based on a modified version of the Pechini method, has since become a popular method of improving sinterability of BZY. The resultant BZY powders are calcined at 1100°C and sintered at temperatures as low as 1600°C for 8 hours [4].

1.5 Non-Perovskite Proton Conductors

Though perovskite materials are the predominant choice for proton conducting electrolytes, there are a few alternatives available. Recently there have been reports of proton conductivity in $LaPO_4$ systems [9, 10]. The PO_4^{3-} is tetrahedrally structured and, similar to perovskites, oxygen vacancies needed to react with water to stimulate proton conductivity [11]. However, many materials of the $LaPO_4$ structure tend to have low conductivities. There have been a number of studies dedicated to the perovskite lanthanum gallates, usually doped with strontium and magnesium (LSGM); these studies have shown LSGM to be a good oxygen-ion conductor. A related material with a K_2NiF_4 structure, $LaSrGaO_4$, has demonstrated low conductivity, but when the strontium dopant is replaced with barium (LBG), the conductivity is enhanced[11]. This structure has an orthorhombic cell with a tetrahedral coordination for gallium, as seen in Figure 1.3 [11].

Through electrochemical impedance spectroscopy (EIS), this new $La_{1-x}Ba_{1+x}GaO_{4-\delta}$ material with $x \leq 0.2$ (LBG 214) was determined to show impressively high proton conductivity, especially for a cell containing tetrahedral moieties [11].

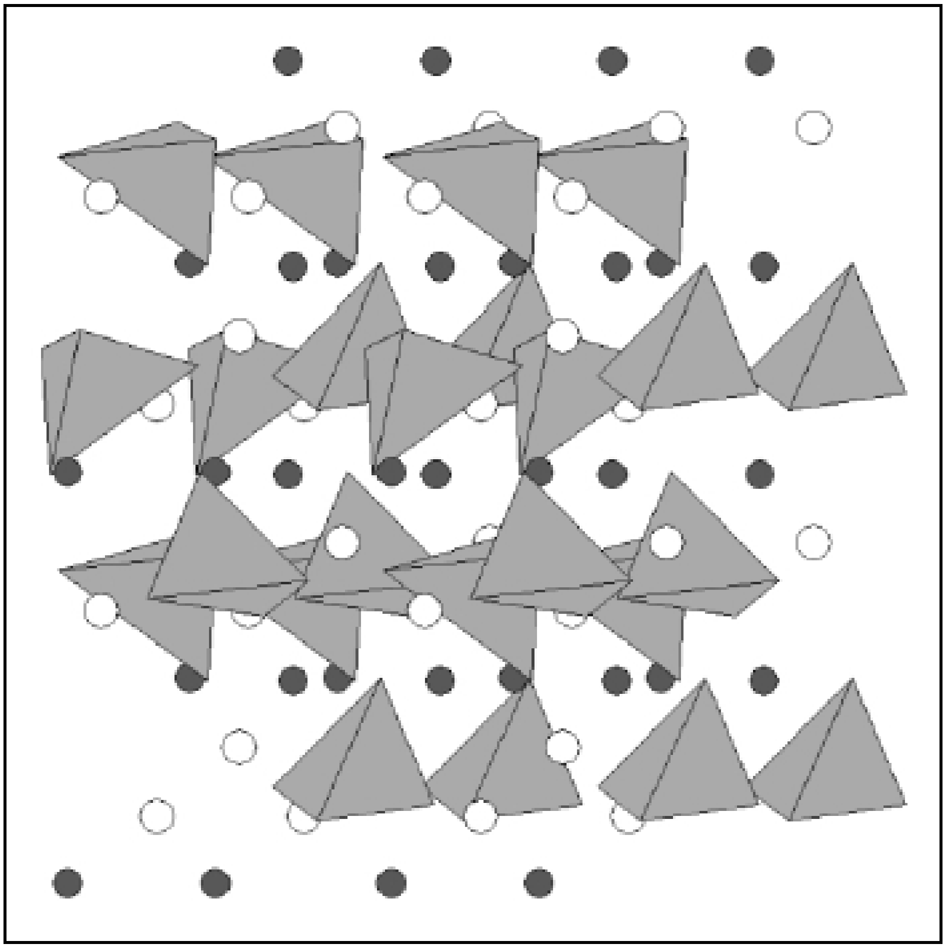

Figure 1.3 $LaBaGaO_4$ structure (La – dark spheres, Ba – light spheres, GaO_4 – tetrahedral) [11]

Though there is high proton conductivity in LBG 214, barium doping is often associated with sintering problems, causing the material to have a low density and conductivity. As previously mentioned, one solution to making the electrolyte denser is through the use of sintering aids. As an alternative to sintering aids, transient liquid phase sintering may be used to make the material denser.

1.6 Transient Liquid Phase Sintering Method

A study conducted on the sinterability of lanthanum chromite suggests the use of dopant calcium oxide as a sintering aid to overcome the difficulty of sintering chrome based oxides to a high density. It was noticed when sintering $La_{0.7}Ca_xCrO_3$ (LCC), a $CaCrO_4$ exsolution appeared in the material and a transient liquid phase appeared at temperatures between 850°C and 1000°C [12]. During the transient liquid phase, $CaCrO_4$ melted, making the material partially dense. A second liquid phase occurred at 1250°C, due to a slight increase in calcium content, causing a near complete densification; afterward the secondary phases dissolved back into the chromite [12].

Using the concept of a transient liquid phase, it may be possible to manipulate LBG 214 to reach a high density without compromising the good proton conductivity of the electrolyte. Already an impressive proton conductor, if LBG 214 can be near complete densification, it could be considered a very important non-perovskite proton conductor for SOFC electrolyte applications. More importantly, if the transient liquid phase concept proves to be a reliable form of densifying electrolyte materials, the concept may be used in the preparation of other electrolytes that have difficulties reaching complete densification.

Yttrium-doped barium zirconate is arguably considered one of the most important electrolyte material utilized in IT-SOFC. Though BZY electrolytes have exemplary electrochemical properties, there is still a need to reduce the cost of synthesis. By further reducing sintering temperatures, and thus reduce price of production, BZY may become a marketable electrolyte for SOFC technology. Many studies have attempted to reduce sintering temperatures through numerous methods, but the sintering process still requires temperatures of at least 1600°C for 8 hours. Using the concept of a transient liquid method, it may be possible to reduce these high sintering temperatures.

1.7 CO_2 Separation Membranes

In 2008 almost 40% of 5.8 billion metric tons of anthropogenic CO_2 emissions in the U.S. was generated through the burning of fossil fuels for electricity [13, 14]. According to the 2008 statistics, the burning of fossil fuels generates about 71% of the electricity used in the United States [13, 14]. Currently, carbon capture and storage (CCS) is the only immediate option for reducing CO_2 emissions and stabilizing CO_2 levels in the atmosphere. Currently the pre-combustion, oxy-fuel combustion, and post-combustion stages of the industrial process stream present in fossil fuel based power plants are the targets of CO_2 separation/capture systems.

Integrated gasification combined cycles (IGCC) power plants can use pre-combustion CCS to remove CO_2 from H_2, which makes up 40% of the mixture [15]. This allows for the combustion of pure H_2. Both pulverized coal (PC) and natural gas-fired power plants utilize either the oxy-combustion or post-combustion CCS. For post-combustion, fossil fuels are combusted in air and produce a flue gas; the CCS is used to remove approximately 14% of CO_2 from this N_2 concentrated flue gas [16, 17]. For oxy-combustion, fossil fuels are combusted in pure oxygen, producing a 60% CO_2-H_2O stream; CO_2 can then be easily separated by condensing H_2O [18].

Current CCS technology requires further development before they can be successfully utilized in fossil fuel based power plants. These CO_2 capture/separation technologies are confined to chemical/physical absorption through the use of liquid solvents or solid sorbents [15]. A parasitic load that uses steam and power is required for cases using post-combustion CCS; this parasitic load causes a substantial decrease, by nearly a third, to the overall power generation of the plant and can cause an increase, by nearly 80%, to the cost of electricity (COE) [19, 20].

When applied to pre and post combustion CO_2 capture, membrane based separation/capture do not require any steam or chemical load. This allows for the delivery of high pressure CO_2 and drives the CO shifting reaction to completion. However, this system has limited selectivity, affecting product purity and causing poor compatibility with high temperature process steam. These shortcomings create a demand for alternative high temperature membrane technology. Mixed ionic/electronic conductor based membranes may be the answer to these current issues with membrane separation/capture systems. Ionic transport membranes only permit the electrochemically active species to transport through the membrane under an electrochemical potential gradient and it usually operates at high temperatures, providing good compatibility with high temperature process stream [15]. Unlike electrically driven molten carbonate fuel cell based CO_2 concentrators for separation, the mixed carbonate-ion/oxide-ion conductor (MOCC) and mixed carbonate-ion/electronic conductor (MECC) dual-phased systems are advantageous both technically and economically because there is no need for external electronic equipment [15].

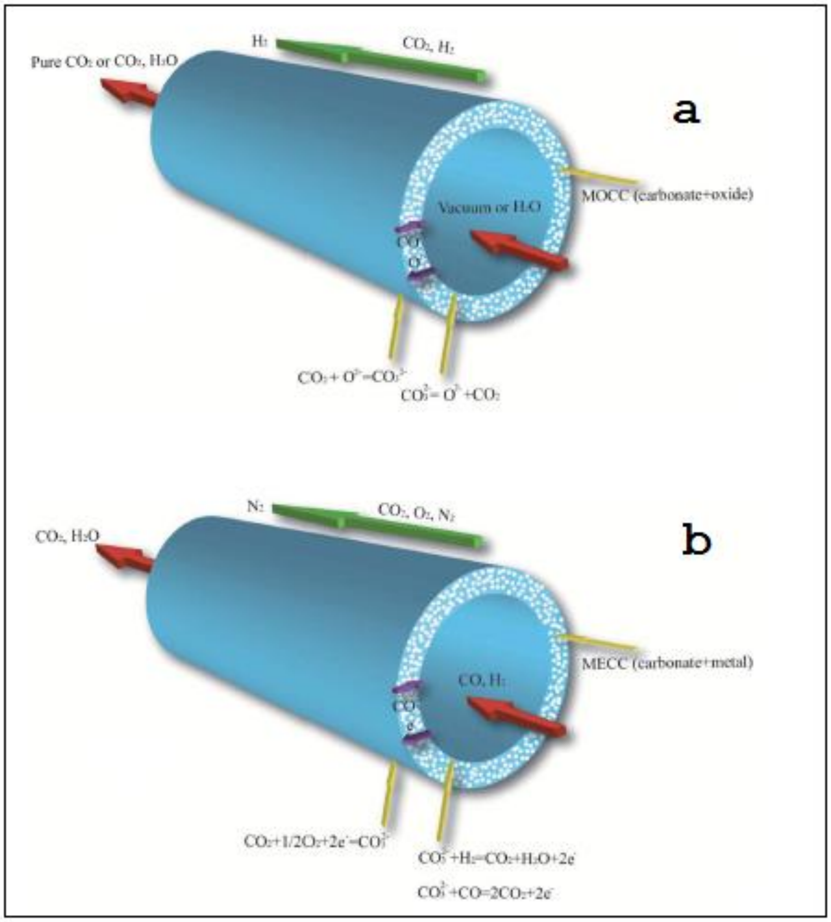

Figure 1.4 a) MOCC working principle, b) MECC working principle [15]

Fundamentally, MOCC is more adequate for separating CO_2 for a reducing stream, CO_2 + H_2; the electrochemical gradients of CO_3^{2-} and O^{2-} exist in opposite directions of the membrane. In the presence of a reducing stream, the O^{2-} will charge balance the CO_3^{2-} across the membrane [15]. MECC is a more adequate solution for CO_2 separation when in the presence of a flue gas: a combination of CO_2, O_2, and N_2. In the case of the MECC, the electrochemical gradients are CO_3^{2-} and e^- [15]. Working principles for both MOCC and MECC are shown in Figure 1.4. There have been suggestions that the CO_2 and O_2 that permeate through the membrane may be recycled back to the combustion chamber for oxy-combustion, or by combusting in a fuel, such as syngas, which may be converted into a pure stream of CO_2 and H_2O. It has been theorized that the heat caused by the highly exothermic fuel oxidation reaction to convert the gas, may be used to produce steam for further electricity production [15].

CHAPTER 2:

DENSIFYING PROTON CONDUCTORS WITH A NOVEL FLUX

2.1 Background

The transient liquid phase sintering method studied in Larry Chick's work on sintering calcium–substituted lanthanum chromite served as a basis in a preliminary study conducted on the densification of $La_{1-x}Ba_{1+x}GaO_{4-\delta}$ (LBG 214). Barium gallate (BG) was chosen as a new flux material to aid in the sintering process.

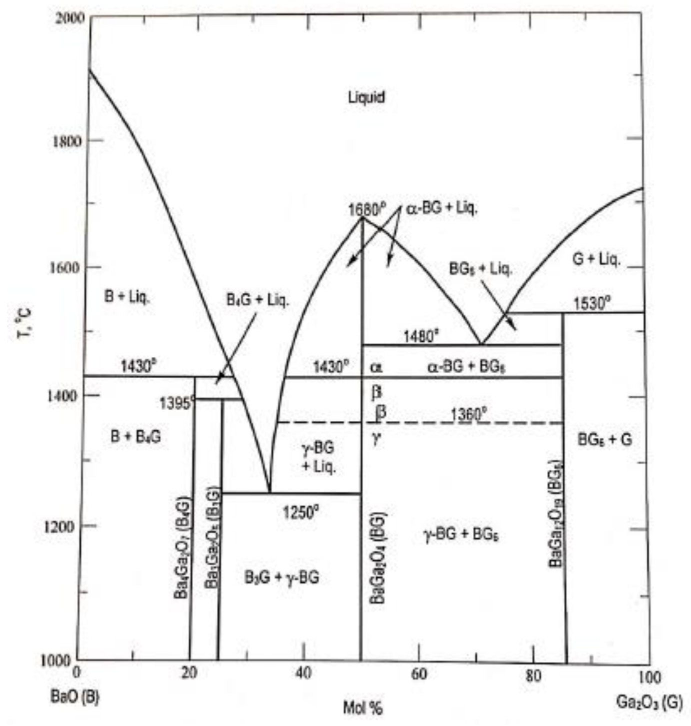

Figure 2.1 BaO/Ga_2O_3 phase diagram.

Theoretically, the use of barium gallate (BG) as a flux should not introduce any impurities into LBG 214 due to common components shared between both materials. According to the phase diagram in Figure 2.1, BG with a composition of 68 Mol% BaO and 32 Mol% Ga_2O_3, has a eutectic temperature at 1250°C, making it ideal for creating a transient liquid phase during the sintering process of LBG 214.

In the preliminary study, BG in fact aided densification during the sintering process of LBG 214. Three different samples were prepared with variation on the weight percentage of BG added to LBG214 (0wt%, 1wt%, and 10wt%). The higher the BG contents in LBG 214, the higher the density. The effects of the BG flux in LBG 214 can be seen in scanning electron microscope images in Figure 2.2.

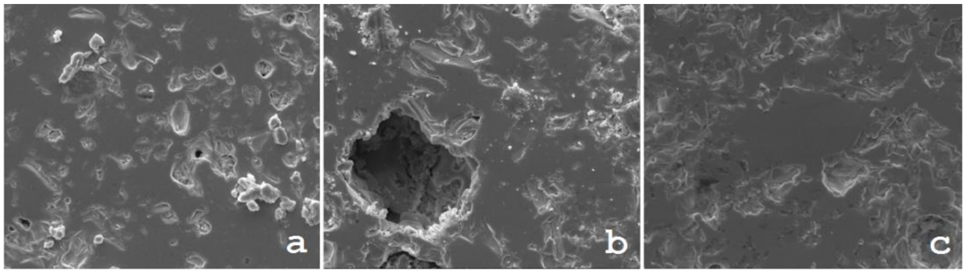

Figure 2.2 Microstructures of a) LBG 214, b) LBG 214-BG 1 wt%, c) LBG 214-BG 10wt%

The techniques for transient liquid phase sintering introduced in the preliminary study serve as a basis for the study on reducing sintering temperatures for BZY20 through a transient liquid phase sintering process.

BZY20 is highly regarded as the most promising HTPC electrolyte material for SOFC technology. Currently, the most advanced techniques for synthesis require high temperatures and long sintering processes, at least 1600°C for 8 hours. In order to make

BZY20 a commercially viable option, these sintering temperatures and times must be reduced.

In the preliminary study conducted on LBG 214, the material was sintered at 1250°C and showed signs of densification. Using barium gallate as a flux to create a transient liquid phase when sintering BZY20, it may be possible to reduce the high sintering temperatures without compromising the material's density. Furthermore, if the transient liquid phase sintering method proves applicable, synthesis through a solid state reaction could become a viable option rather than the more complex and predominantly used wet chemical synthesis methods.

2.2 Experimental

Yttrium-doped (20mol%) barium zirconate (BZY20) powder was synthesized through solid state reaction using stoichiometric quantities of commercial $BaCO_3$, ZrO_2, and Y_2O_3. Barium Gallate (BG) powder was synthesized similarly using stoichiometric amounts of commercial $BaCO_3$ and Ga_2O_3; the resultant BG powder was calcined at 1250°C for 5 hours. The resultant BZY20 powder was calcined at 1200°C for 1 hours and ball milled in ethyl alcohol, before being calcined a second time at 1400°C for 10 hours.

After calcination, BZY20 was mixed with various weight percentages of BG powder: 0wt%, 1wt%, 10wt%, 20 wt%, 30wt%, and 50wt%. The BZY20-BG powders were all mixed with 1wt% of polyvinyl butyral for binding and were uniaxially pressed under 5 tons of pressure into bar samples. Due to the melting temperature of BG being 1250°C, the BZY-BG bar samples were the sintered at 1300°C for 10 hours to ensure the presence of a transient liquid phase within each sample. A heating rate of 3°C/min. was used for all calcinations and sintering processes. X-ray diffraction was used to analyze the phase composition for synthesized samples, XRD was conducted using a Rigaku Miniflex II.

To analyze the electrochemical properties of the various BZY20-BG samples, electrochemical impedance spectroscopy (EIS) was us conducted using a Solartron SI 1260 Impedance/Gain-Phase Analyzer coupled with a SI 1287 Electrochemical Interface and a Zahner Elektrik I-M6. All EIS analyses were conducted using a frequency range of $1x10^6$ Hz to 0.1 Hz and a stimulus voltage of 10 mV. Bar samples were prepared with silver paste and meshing electrodes, then heated to 700°C at a rate of 3°C/min for half-cell testing. EIS testing was conducted at temperature range from 400°C to 700°C at 50°C intervals under dry and wet atmosphere conditions of 2.78%, 5.57%, and 10.51% pH_2O. All samples were analyzed using four-probe AC impedance measurements.

To study the effect BG has on the densification of BZY20, a combination of thermomechanical analysis (TMA) and Archimedes' principle were utilized. Bars of unsintered BZY20-BG were prepared and TMA was conducted using a Netzsch Dilatometer 402 with a heating rate of 3°C/min. until reaching 1300°C, then hold temperature constant for 10 hours before reducing back to room temperature. The percentage of total density reached was determined using sintered BZY20-BG samples and equations governed by Archimedes' principle.

$$V_p = \frac{M_{wet} - M_{dry}}{\rho_{liq}} \qquad 2.1$$

$$V_{total} = V_s - V_p \qquad 2.2$$

$$\rho_{\%} = 1 - \frac{V_p}{V_s} \qquad 2.3$$

Equation 2.1 represents the calculated volume of pores within a sample (V_p), using the mass of a sample infiltrated with a liquid (M_{wet}) the mass of the dry sample (M_{dry}) and the density of the liquid (ρ_{liq}) used for infiltration. The volume of solid (V_s) within a sample can be found from the volume of pores and the total volume, found through geometry. After obtaining both V_s and V_p, the density percentage may be calculated from Equation 2.3.

BZY20-BG bars were fractured and sputtered with Au using a Denton Desk II Sputter Coater for SEM imaging. A Zeiss Ultra Plus scanning electron microscope (SEM) was then utilized in studying the morphology and density of the samples' cross section.

2.3 Results and Discussion

BZY20 powders were synthesized with 0wt%, 1wt%, 10wt%, 20wt%, 30wt%, and 50wt% of BG powder. Figure 2.3 displays x-ray diffraction patterns for BZY20 with BG variations sintered at 1300°C for 10 hours. For comparison, the cubic perovskite structure of barium zirconate was included with the diffraction patterns. Diffractograms for BZY20 samples sintered using a BG content of 50wt% contains several small peaks suggesting signs of impurities. Indicators for BG peaks have been included as a possible explanation for these impurities due to a larger BG content. The diffractogram for BZY20-BG 30wt% has an extra peak at approximately 2ɵ = 78°.

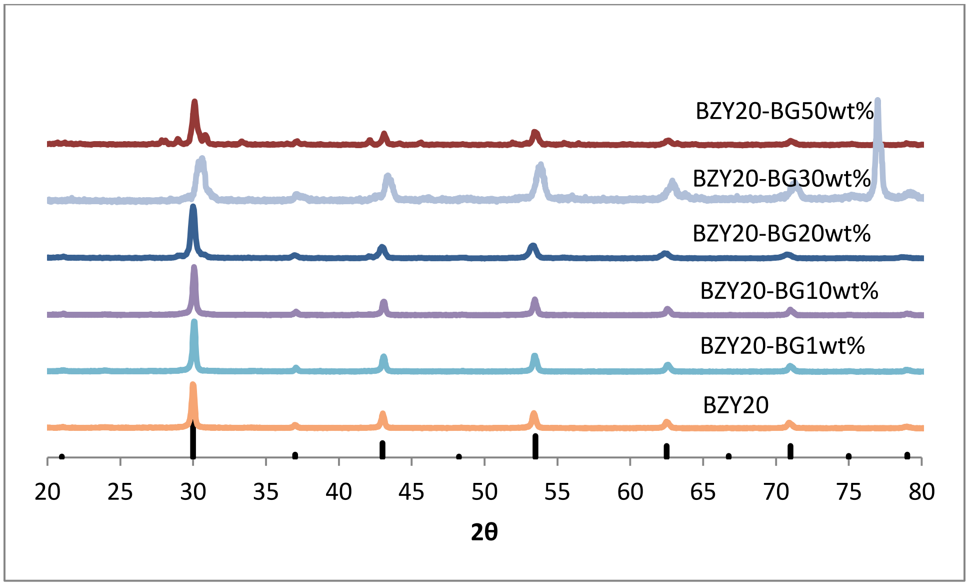

Figure 2.3 XRD spectra for BZY20-BG 0wt%, 1wt%, 10wt%, 20wt%, 30wt%, and 50wt%.

Samples sintered with a BG content of 10wt% or smaller were structurally compromised due to the low sintering temperature of 1300°C. For this reason, samples sintered with low amounts of BG could not be analyzed using SEM, EIS, or TMA techniques.

Thermomechanical analysis curves for BZY20 samples sintered with 20wt%, 30wt%, and 50wt% of BG were included in Figure 2.4. This data shows the change in stretch ratio (dλ) of BZY20-BG bar samples over the time duration (min.) for sintering the bars at a constant temperature of 1300°C. The data suggests a greater shrinkage in samples containing larger amounts of BG. Based on the data, it is possible to suggest the bulk of shrinkage in the sintered samples occurs within the first 4 hours of sintering.

There is slightly less shrinkage seen in the tested BZY20-BG 30wt% sample, when compared with BZY20-BG 20wt%. The presence of internal fractures during the sintering process is a potential explanation for the smaller shrinkage in this sample.

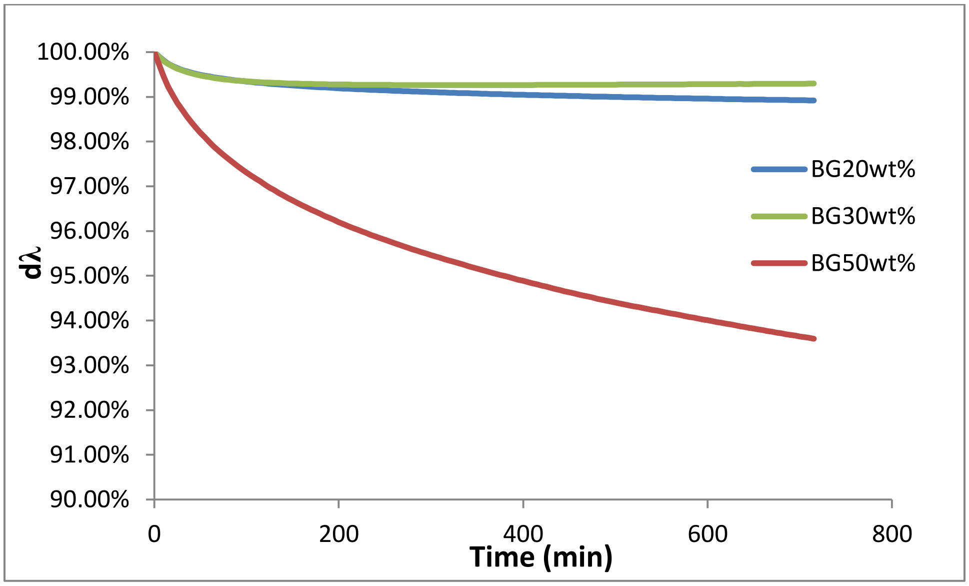

Figure 2.4 Thermal shrinkage profiles for BZY20 with BG content at 20wt%, 30wt%, 50wt%

Using Archimedes principle for determining density and scanning electron microscope images, it was possible to characterize and analyze the densification for BZY20-BG samples. In Figures 2.6 through 2.8, SEM images are compared for fractured BZY20-BG samples with BG 20wt%, 30wt%, and 50wt%. For the sake of comparison, an SEM image of fractured BZY20 prepared via solid state reaction, sintered at 1500°C was included in Figure 2.5 a) [21]. As suggested in the TMA testing, the samples sintered with higher BG weight percentage tend to reach a more dense state. To further verify this trend, Archimedes principle was used to calculate density percentages for the sintered samples, included in Table 2.1.

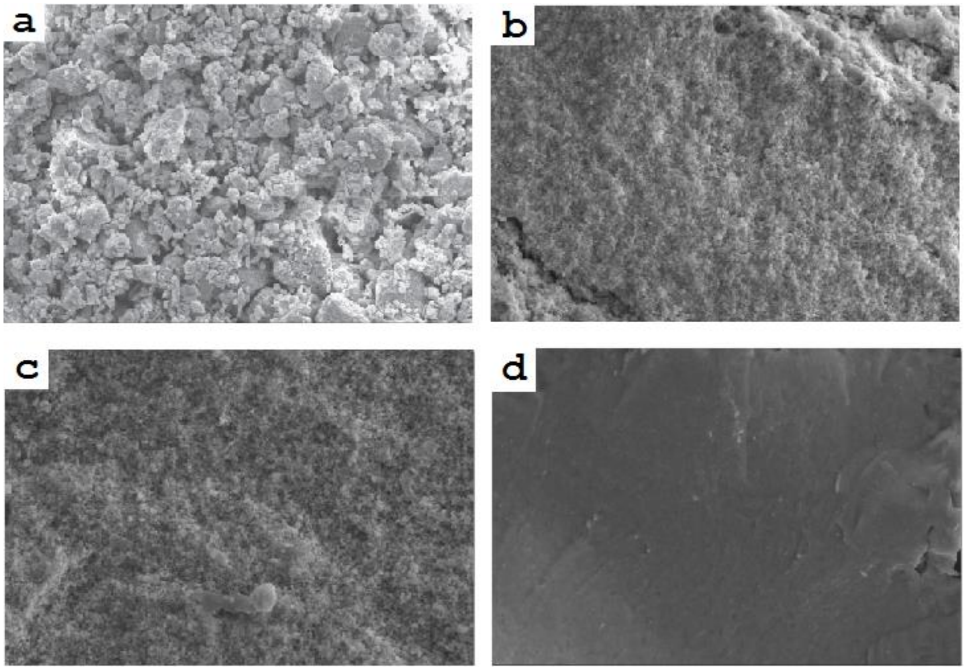

Figure 2.5 SEM photographs of BZY20 with a) BG 0wt% sintered at 1500°C under 4000x magnification [21], b) BG 20wt%, c) BG 30wt%, d) BG 50wt% sintered at 1300°C under 5000x magnification.

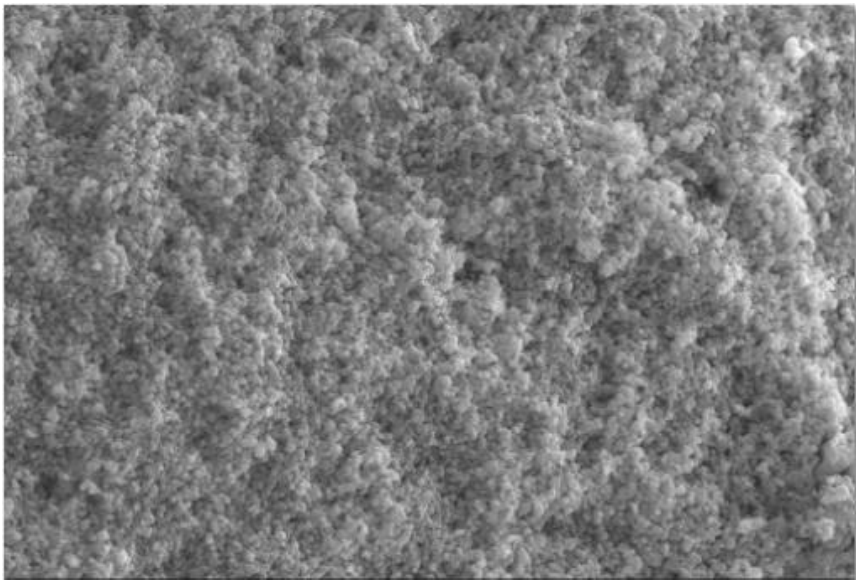

Figure 2.6 Microstructures of BZY20 with BG 20wt% at 10k magnification

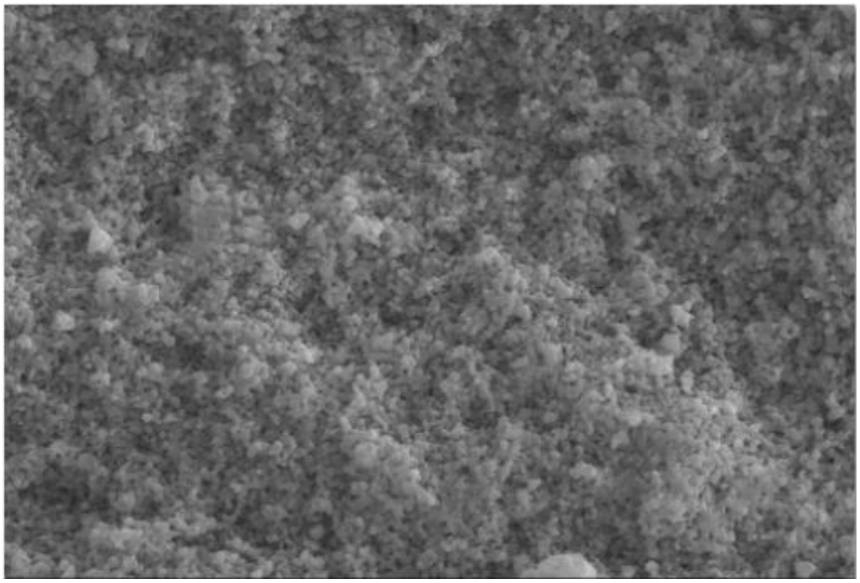

Figure 2.7 Microstructures of BZY20 BG 30wt% at 10k magnification

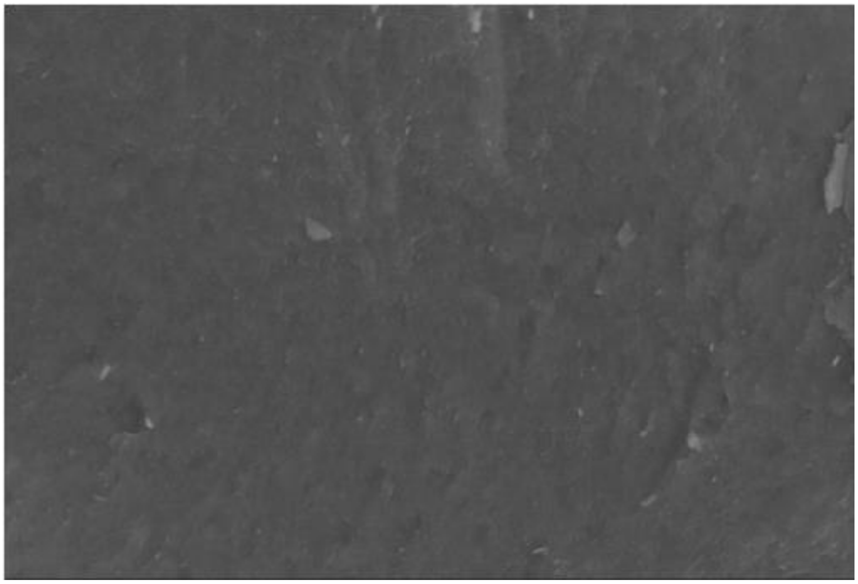

Figure 2.8 Microstructures of BZY20 BG 50wt% at 10k magnification

Table 2.1 Sample density calculated from Archimedes principle

Condition	BG 20wt%	BG 30wt%	BG 50wt%
ρ	55%	63%	69%

Electrochemical impedance spectroscopy was conducted on BZY20-BG samples of 20wt%, 30wt%, and 50wt% over a frequency range of $1x10^6$ to 0.1 Hz. Figures 2.9 through 2.11 show Arrhenius plots for these different BZY20-BG samples with variations in temperature, ranging from 400°C to 700°C, and variations in atmospheric humidity. These atmospheres contained partial pressures of H_2, pH_2O of 2.78%, 5.57%, and 10.51%; EIS testing was also conducted under a completely dry atmosphere. Proton conduction dominates at lower temperatures; this trend is particularly noticeable in BZY20-BG 20wt% and 30wt%. Proton conductors also tend to excel under wet atmospheres. In these BZY20-BG samples, this trend mostly holds true, with the exception of 10.51% pH_2O. At this atmosphere, the conductivities drop slightly below the conductivities observed for samples tested under the 5.57% pH_2O atmospheric condition. A potential reason for this observation could be the addition of barium gallate that is hindering the proton conductivity at these elevated humidity's. Generally, proton conductivity tends to excel when introduced to atmospheres containing large amounts of water; however, with the addition of BG it may be possible for the proton conductivity to plateau after a certain percentage of water is introduced to the atmosphere.

For all of the BZY20-BG impedance spectra, BG 20wt% under 5.57% pH_2O for temperatures 550°C to 700°C is included in Figure 2.12 and 400°C to 550°C in Figure 2.13, the lower frequency arcs appear to be nonexistent. However, at the temperatures lower than 550°C, a second arc begins to grow. This behavior is considered quite unusual for proton conducting electrolytes. One possible explanation is the resistance attributed to the grain boundary may have been reduced due to the addition of low melting phase BG.

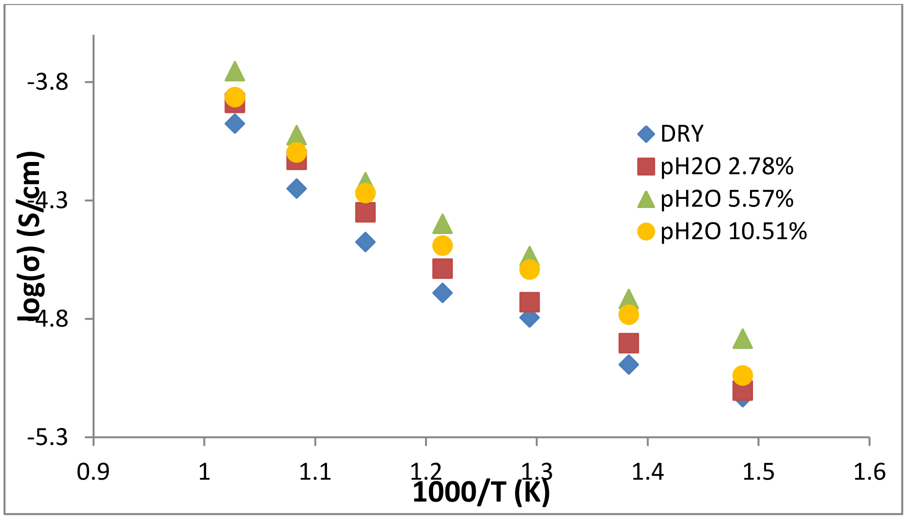

Figure 2.9 Arrhenius plot of ionic conductivity of BZY20-BG 20wt%.

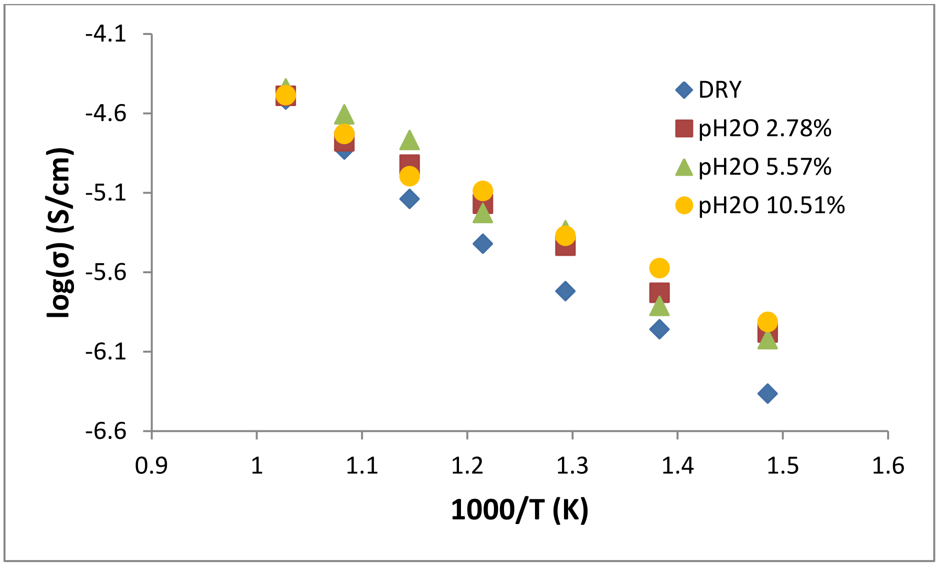

Figure 2.10 Arrhenius plot of ionic conductivity of BZY20-BG 30wt%.

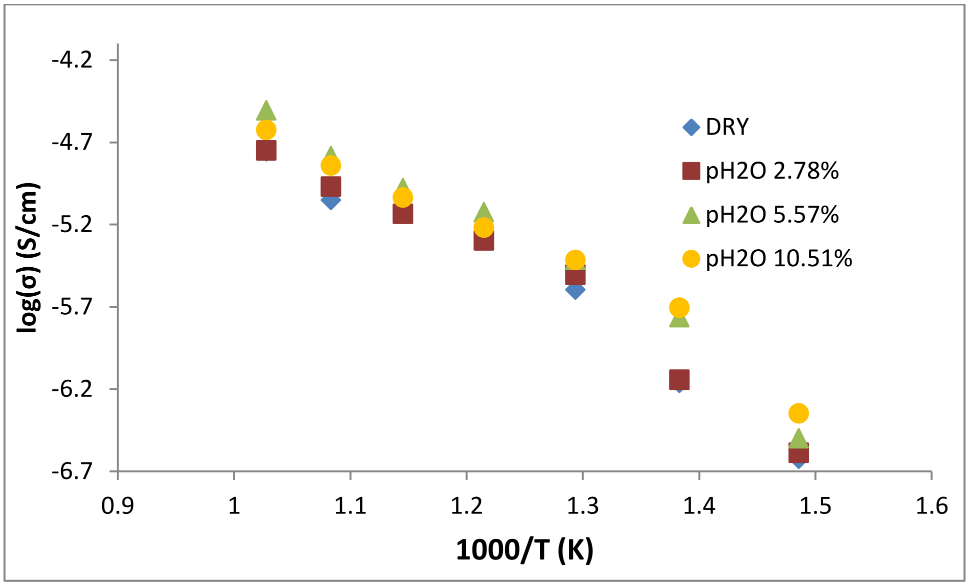

Figure 2.11 Arrhenius plot of ionic conductivity of BZY20-BG 50wt%.

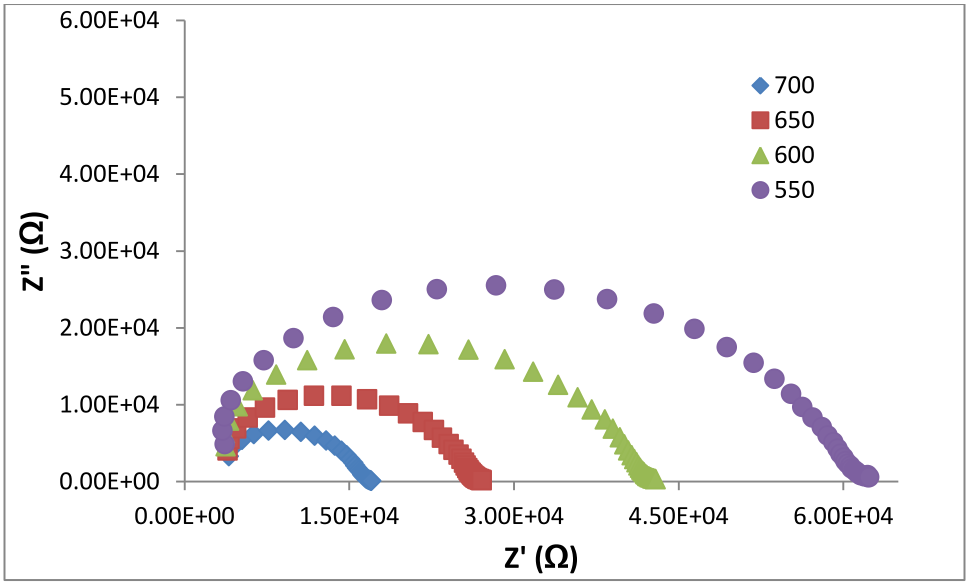

Figure 2.12 Impedance spectra for BZY20-BG 20wt% under pH_2O 5.57% atmosphere for temperatures 550°C-700°C.

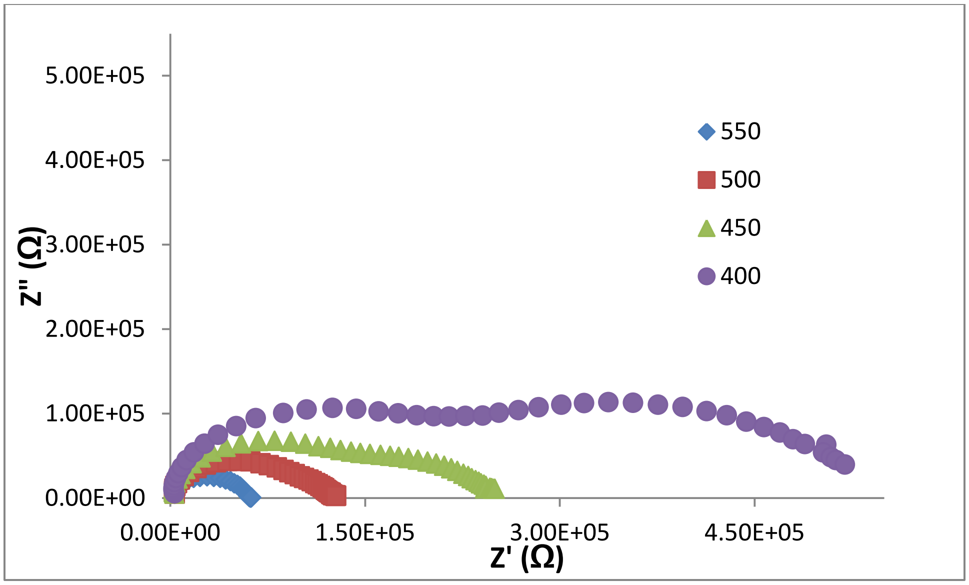

Figure 2.13 Impedance spectra for BZY20-BG 20wt% under pH_2O 5.57% atmosphere for temperatures 400°C-700°C.

Using the data given in these Arrhenius plots, Table 2.2 was constructed comparing calculated activation energies for the three BZY20 samples. BZY20-BG 20wt% shows the lowest activation energy; an activation energy of 0.47eV under a humid atmosphere of 5.57% pH_2O. Lower activation energy with less BG implies prevalent proton conduction in these materials.

Table 2.2 Activation energies for all BZY20-BG samples.

Condition	DRY	2.78% pH_2O	5.57% pH_2O	10.51% pH_2O
BG20wt%	0.48	0.51	0.47	0.48
BG30wt%	0.78	0.64	0.59	0.72
BG50wt%	0.78	0.78	0.80	0.69

In Figures 2.14 through 2.18, conductivity of the various BZY20 samples are plotted against the increasingly humid atmospheres and a constant temperature for each plot. Temperatures chosen for these plots include 700°C, 600°C, 500°C, and 400°C. These figures clearly demonstrate that BZY20-BG 20wt% samples outperform other BZY20 samples sintered with BG at all tested temperatures and test atmospheres. These plots reaffirm conductivity drops, or remain relatively constant, in atmospheres containing humidity higher than 5.57% pH_2O. The data presented here implies samples with a lower BG content tend to display higher proton conductivities; the samples synthesized with 20wt% of BG generally show an increase in conductivity of approximately 3 S/cm higher than samples synthesized with 30wt% or 50wt% of BG.

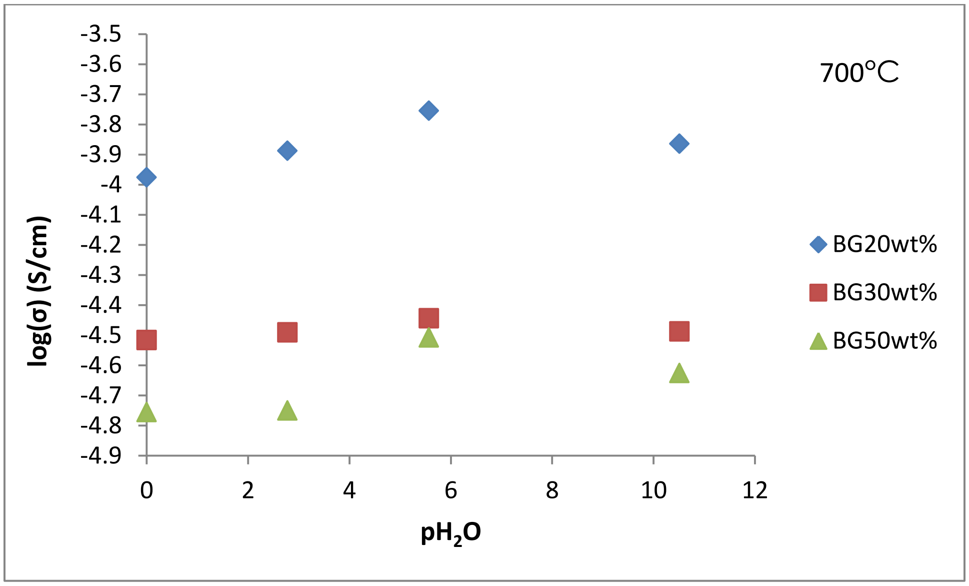

Figure 2.14 Conductivity plotted against variable atmospheric conditions for data taken at 700°C.

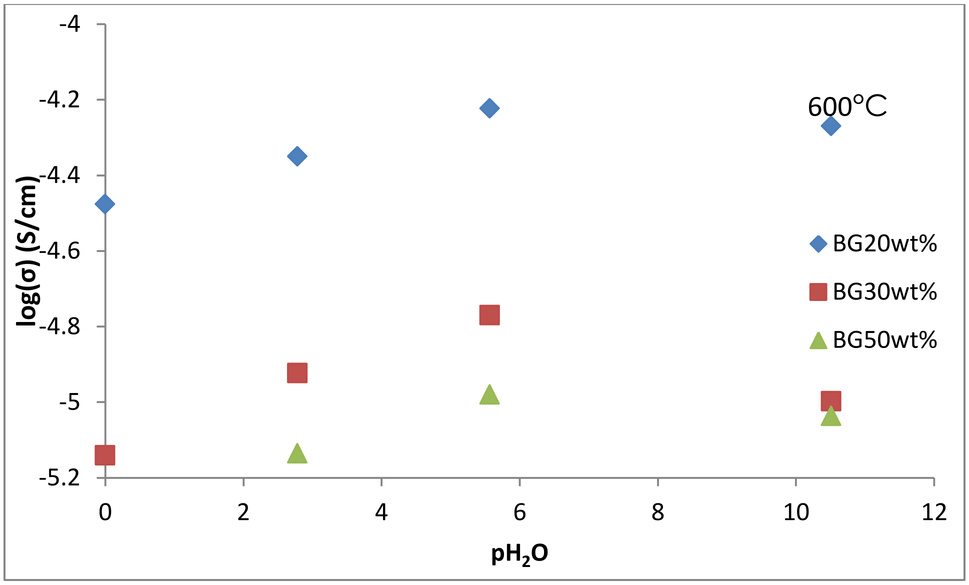

Figure 2.15 Conductivity plotted against variable atmospheric conditions for data taken at 600°C.

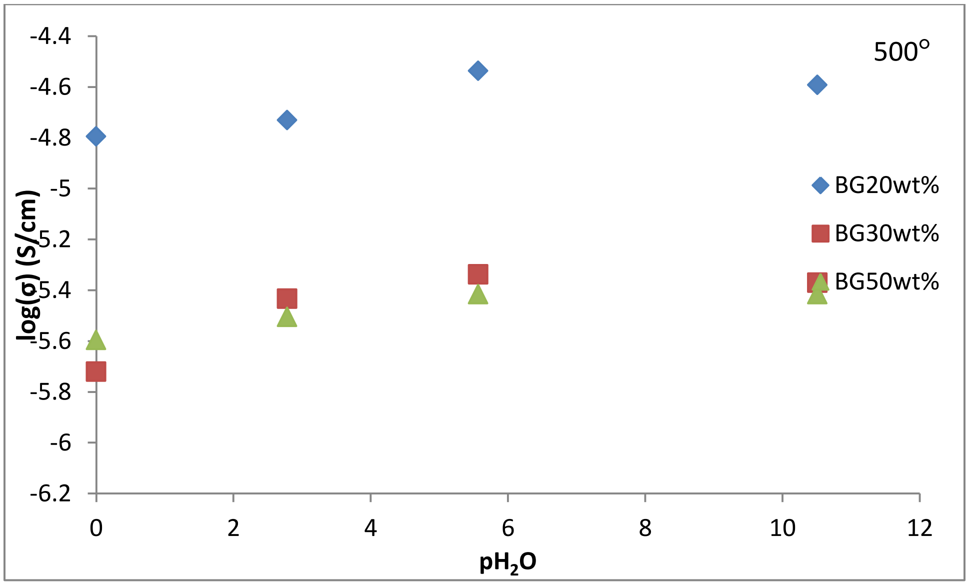

Figure 2.16 Conductivity plotted against variable atmospheric conditions for data taken at 500°C.

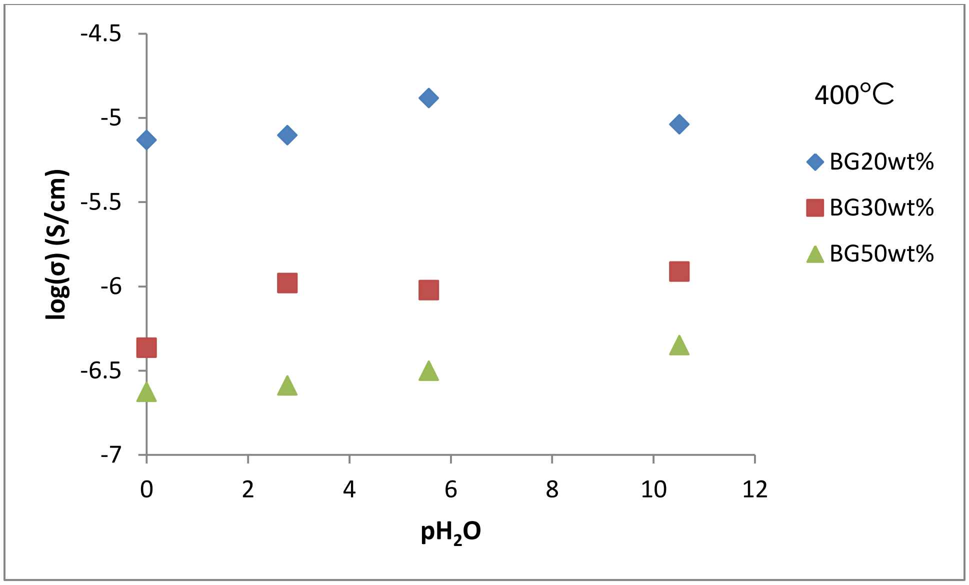

Figure 2.17 Conductivity plotted against variable atmospheric conditions for data taken at 400°C.

Arrhenius plots displaying data for all three BZY20-BG samples under a particular atmosphere are presented in Figures 2.18 through 2.21. From these plots, there is a noticeably higher conductivity for BZY20 samples sintered with 20wt% of BG, thus it is clear BZY20-BG 20wt% outperformed samples with higher BG contents under all tested conditions. Due to BG hindering proton conductivity, it is clear that a lower BG content will yield a higher conductivity for BZY20 samples.

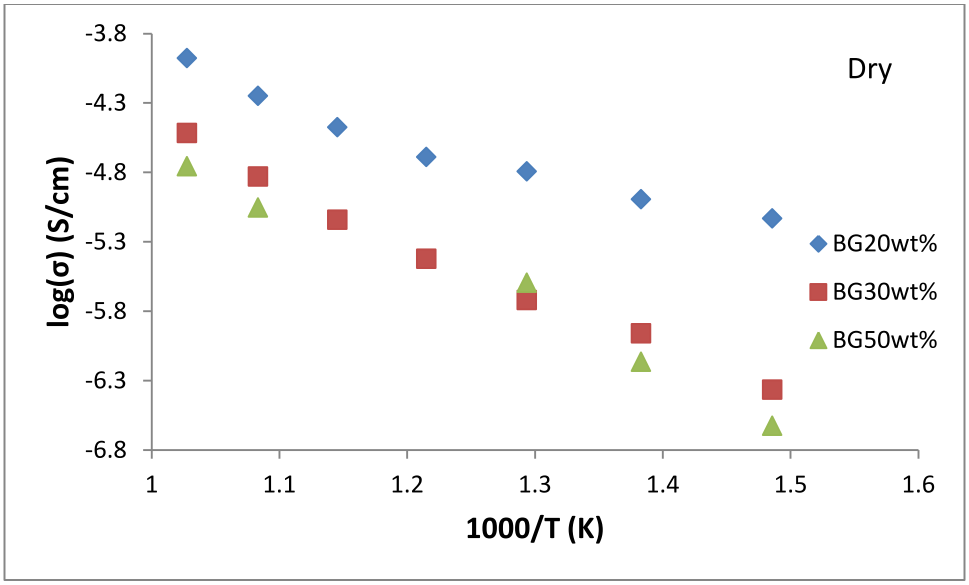

Figure 2.18 Arrhenius plot of ionic conductivity for BG 20wt%, 30wt%, and 50wt% under dry atmosphere.

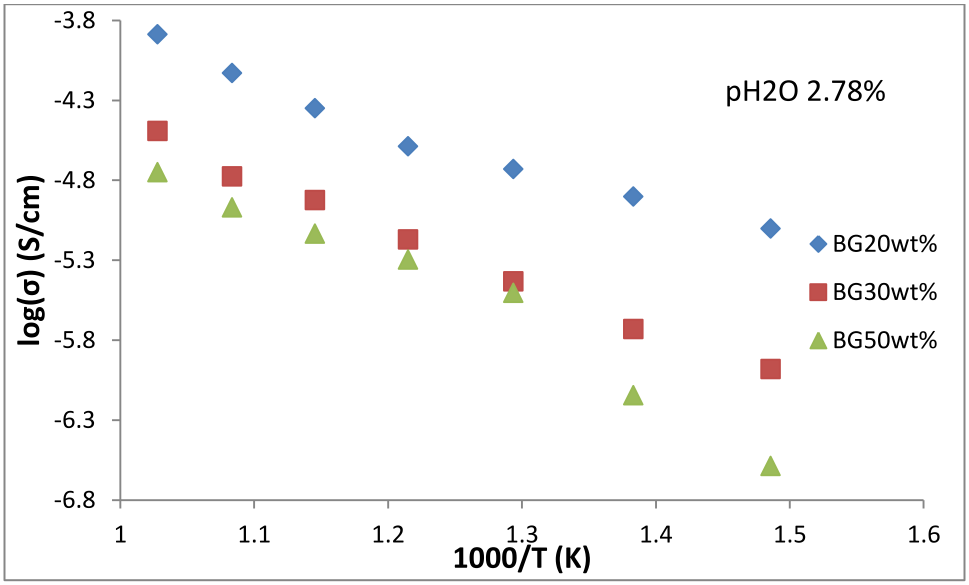

Figure 2.19 Arrhenius plot of ionic conductivity for BG 20wt%, 30wt%, and 50wt% under 2.78% pH_2O.

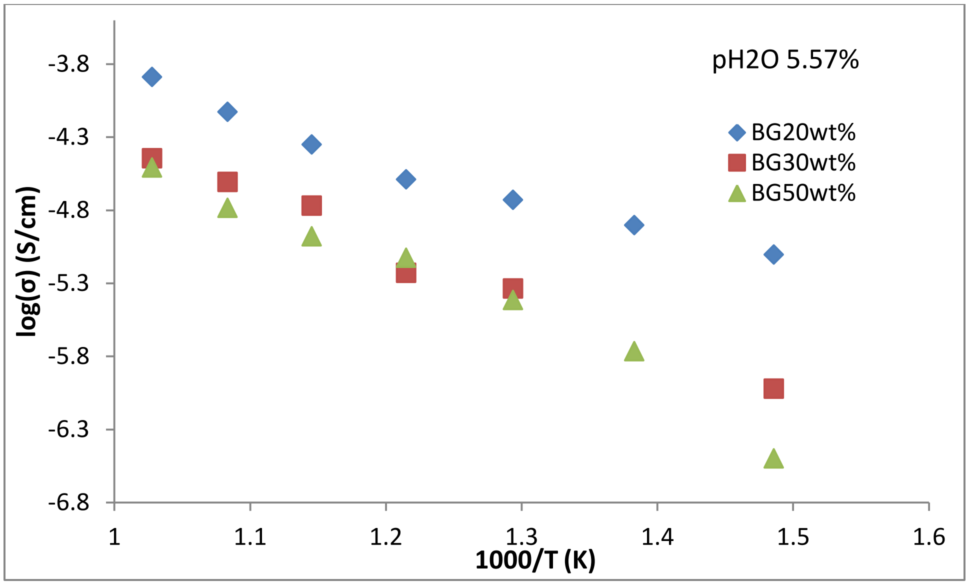

Figure 2.20 Arrhenius plot of ionic conductivity for BG 20wt%, 30wt%, and 50wt% under 5.57% pH_2O.

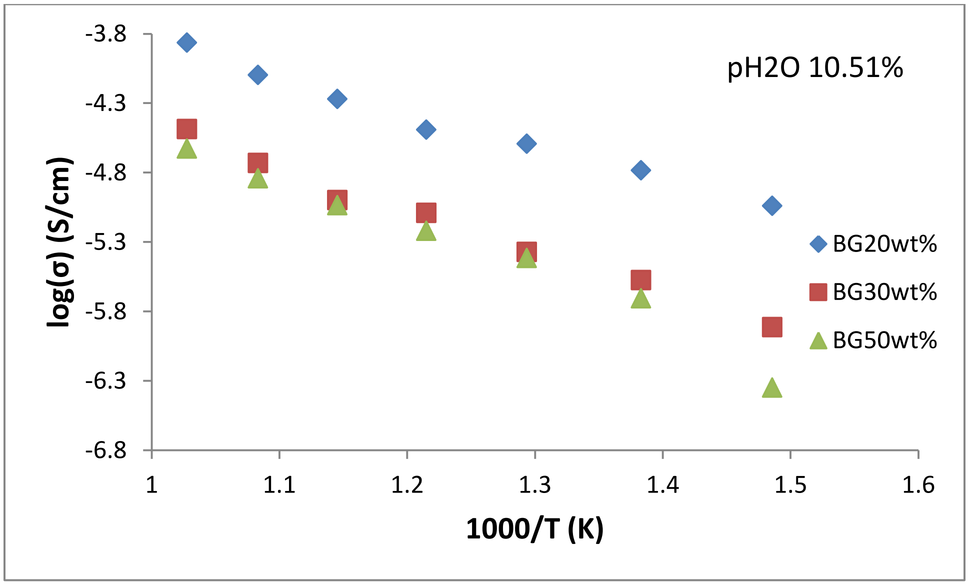

Figure 2.21 Arrhenius plot of ionic conductivity for BG 20wt%, 30wt%, and 50wt% under 10.51% pH_2O.

CHAPTER 3:

A NEW OXIDE-ION CONDUCTOR

3.1 Background

The solid oxide-ion electrolyte is responsible for many aspects of solid oxide fuel cell functionality. The cathode reduces O_2 to $2O^{2-}$; these ions are then transported to the anode, where H_2 is oxidized, via solid oxide-ion electrolyte. During this process the electrolyte is responsible for blocking electron transport within the cell. Aside from the electrolyte mechanisms the cell relies on, the power output is partially dependent on the oxide-ion conductivity of the electrolyte.

In most cases, oxygen-deficient fluorite and perovskite structures are used for oxide-ion conducting electrolytes; this is due to the promotion of oxygen transport through oxygen vacancies in the material [22-24]. Though to a lesser extent, apatite, sheelite, Ruddlesden-Popper, and mayenite structures are also used as oxide-ion electrolytes through the promotion of oxygen transport via interstitial oxide-ions.

In "$Sr_{1-x}K_xSi_{1-y}Ge_yO_{3-0.5x}$: a new family of superior oxide-ion conductor," P. Singh discusses a new design principle for oxide-ion electrolytes. By substituting K^+ for Sr^{2+} in $SrMO_3$ (M = Si or Ge), terminal-oxygen vacancies can be introduced to the material [24]. The studied material contains closed-packed planes of Sr^+ ions separating (001) planes of M_3O_9 formed by three corner-shared MO_4 tetrahedral-anion complexes [24]. Due to steric hindrance of large Sr^{2+} and K^+ ions, these vacancies are not accommodated by corner sharing with neighboring M_3O_9 units [24]. Using steric hindrance to stabilize a terminal-oxygen vacancy in a tetrahedral anion complex represents a new design principle.

In a letter presented by *Nature Materials*, E. Kendrick discusses the role of gallium in electrolyte materials and the effects seen in oxide-ion and proton conduction. Through a combination of experimental and modeling techniques with a focus on $La_{1-x}B_{1+x}GaO_{4-x/2}$, the formation of Ga_2O_7 defects were accommodating oxide-ion vacancies within the material's structure. In this study, oxide-ion conduction would occur through a "cog-wheel" process where the Ga_2O_7 defects would break down and reform while the oxide-ions rotate about the GaO_4 tetrahedrons found in the structure [25]. In conclusion, it is believed that similar mechanisms may relate to the ionic conduction in other oxide-ion systems containing tetrahedral moieties; leading to gallium being a potential replacement for germanium found in $Sr_{1-x}K_xSi_{1-y}Ge_yO_{3-0.5x}$ proposed by P. Singh.

From P. Singh's work, the $Sr_{0.8}K_{0.2}Si_{0.5}Ge_{0.5}O_{2.9}$ compound performed well in the tested intermediate range of temperatures, 600°C to 800°C. The conductivity was found to be as low as $4.38x10^{-3}$ S/cm and displayed an activation energy of 0.67eV at the high temperature region and 1.16eV at the low temperature region [24]. Naturally, this compound was chosen for the study substituting the germanium component for that of gallium; the resulting compound studied being $Sr_{0.8}K_{0.2}Si_{1-y}Ga_yO_{3-\delta}$.

3.2 Experimental

The B-site dopant was varied using 10%, 20%, and 30% of gallium. These variations were due to the need for accommodating the relatively large gallium atoms. The percentages were chosen using the atomic radii of Ga_2O_3 and SiO_2 as a guideline.

For these samples the A-site dopant remained fixed at x = 0.2 in order to draw comparisons with the $Sr_{0.8}K_{0.2}Si_{0.5}Ge_{0.5}O_{2.9}$ baseline.

P. Singh's procedure for synthesis was used as a guideline for all samples. Through the utilization of a solid-state reaction, stoichiometric amounts of $SrCO_3$, K_2CO_3, SiO_2, and GeO_2 or Ga_2O_3 were mixed and heated at 1100°C for 15 hour. These resultant powders were pressed into bar samples under 5 tons of pressure with 1wt% of polyvinyl butyral (PVB). All bar samples were sintered at 1000°C for 20 hours. Bar samples used in electrochemical impedance spectroscopy (EIS) analyses were sanded and fitted with platinum electrode paste and meshing for half-cell testing. Impedance spectra were gathered using a Zahner Elektrik IM-6. All sintering and heating processes utilized a heating rate of 3°C/min.

All four samples went through x-ray diffraction analysis using a Rigaku Miniflex II XRD. All samples were analyzed with a Zeiss Ultra Plus scanning electron microscope (SEM) to characterize the cross section of each sample. SEM samples had a gold coating added to help with the charging effect of the material using a Denton Desk II Sputter Coater. Electrochemical impedance spectroscopy was performed using four-probe AC impedance for all studied samples; using a temperature range of 400°C to 800°C at 50°C intervals. All atmospheres for EIS analysis were under a single dry condition under frequencies $1x10^6$ Hz to 0.1 Hz and 10 mV.

3.3 Results and Discussion

Although the diffractogram spectra of $Sr_{0.8}K_{0.2}Si_{0.5}Ge_{0.5}O_{2.9}$ and $Sr_{0.8}K_{0.2}Si_{1-y}Ga_yO_{3-\delta}$ (y = 0.1, 0.2, 0.3) remain relatively unchanged, there is a noticeable change in intensities for peaks seen in the Ga = 0.2 and 0.3 samples, Figure 3.1. It may be possible that secondary formation created through a higher gallium content could be the cause of these intensity changes.

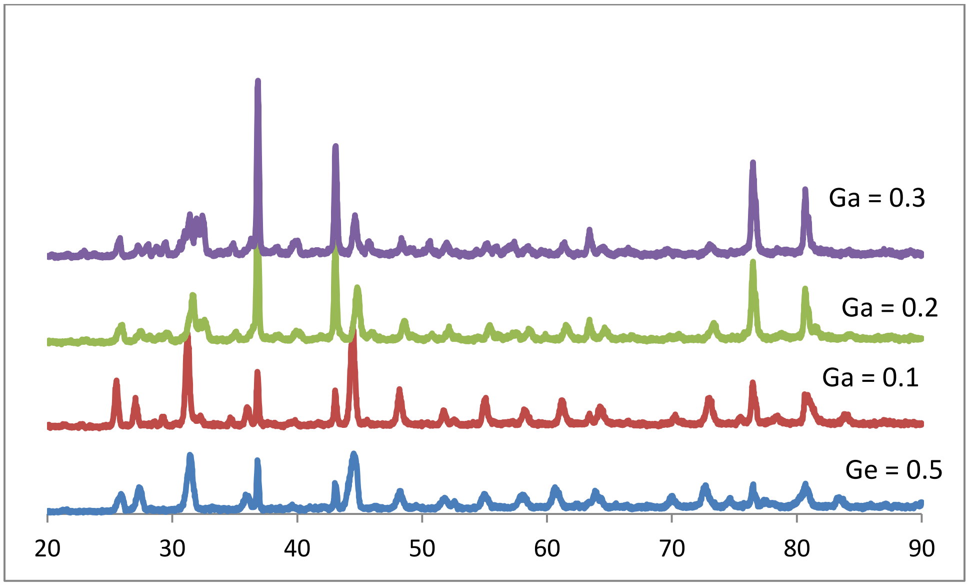

Figure 3.1 XRD spectra for $Sr_{0.8}K_{0.2}Si_{0.5}Ge_{0.5}O_{2.9}$ and $Sr_{0.8}K_{0.2}Si_{1-y}Ga_{y}O_{3-\delta}$ (y = 0.1, 0.2, and 0.3).

Similar to the trend in the diffractograms, there is a noticeable difference seen in the SEM images for the Ga = 0.2 and 0.3 samples, shown in Figure 3.2. While the Ge = 0.5 and Ga = 0.1 are relatively similar, the Ga = 0.2 and 0.3 tend to have an issue with electric charging, making it difficult to obtain clear images of the samples' cross-sections. In these latter two samples, there also appears to be a second formation within the material that was not seen in Ge = 0.5 or Ga = 0.1. The new samples utilizing gallium seem to grow denser with higher gallium content; however, the baseline sample seems, to a much greater extent, less porous than the proposed materials.

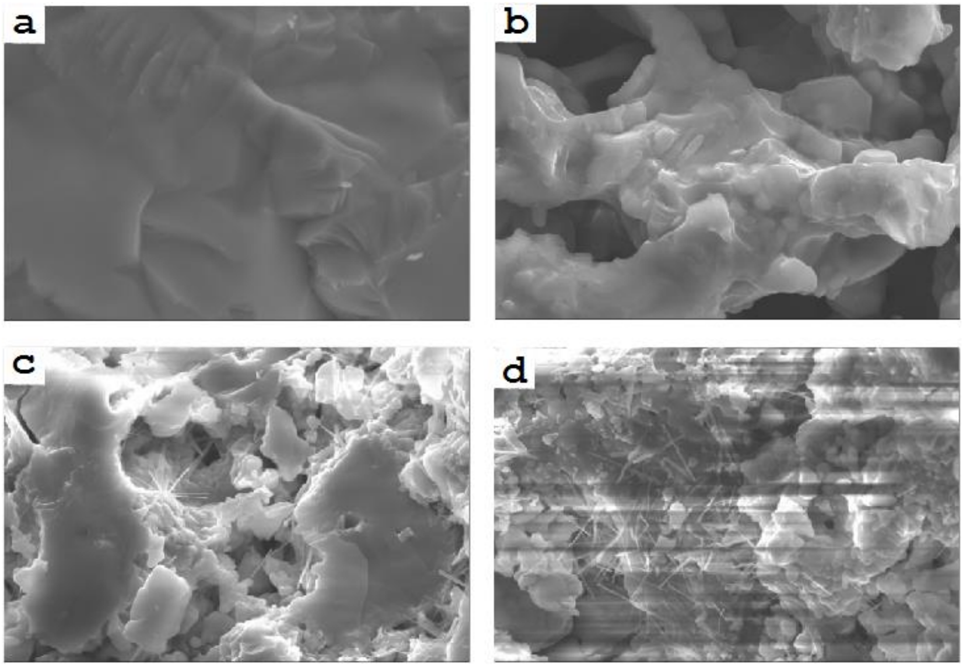

Figure 3.2 SEM images of microstructures of a) $Sr_{0.8}K_{0.2}Si_{0.5}Ge_{0.5}O_{2.9}$, and $Sr_{0.8}K_{0.2}Si_{1-y}Ga_yO_{3-\delta}$ b) Ga = 0.1, c) Ga = 0.2, d) Ga = 0.3 at 10k magnification.

The data gathered from EIS was used in creating an Arrhenius plot, Figure 3.3, for comparing the baseline sample to the new samples utilizing gallium rather than germanium. It should be noted that the tested baseline sample underperformed by nearly an entire order of magnitude when compared with the previously reported conductivity [24]. At 800°C, the observed conductivity for the tested baseline was approximately 7.12×10^{-3} S/cm, where the previously reported conductivity under the same conditions was 4.38×10^{-2} S/cm [24]. From the Arrhenius plot, it is clear that as the gallium content is increased, the sample conductivity decreases. This observation may be attributed to the secondary phase formations seen in SEM analysis. These new formations appear to charge when under SEM analysis and may be the cause for these lower conductivity readings.

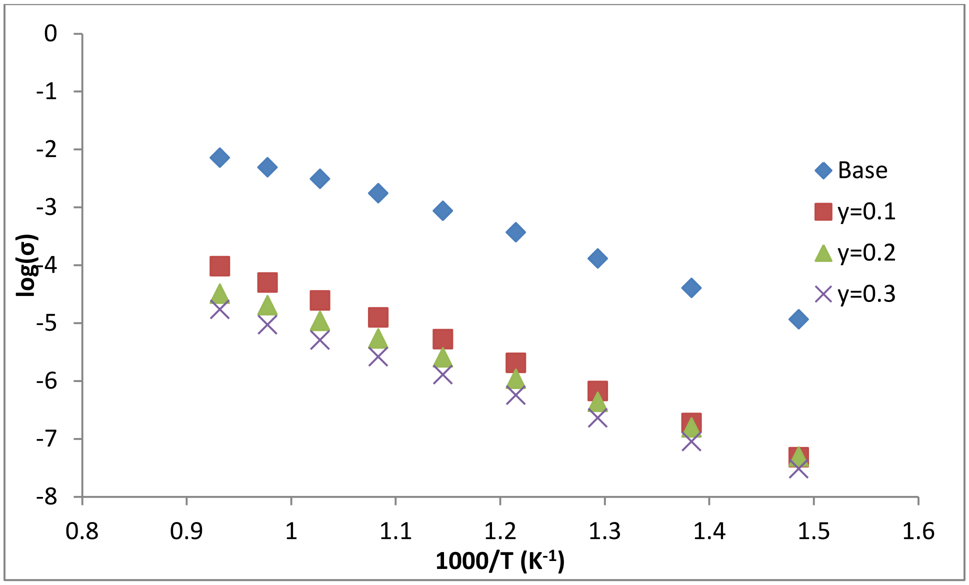

Figure 3.3 Arrhenius plot of ionic conductivity for $Sr_{0.8}K_{0.2}Si_{0.5}Ge_{0.5}O_{2.9}$ and $Sr_{0.8}K_{0.2}Si_{1-y}Ga_{y}O_{2.9}$ (y = 0.1, 0.2, and 0.3).

CHAPTER 4:

IMPROVING MIXED ELECTRON AND CARBONATE ION CONDUCTOR FOR CO_2 CAPTURE MEMBRANES

4.1 BACKGROUND

In order to restore balance to the Earth's atmosphere, CO_2 separation/capture membranes may be the most promising immediate option for achieving this goal. Current research has focused primarily on using solvent/sorbent based CO_2 capture processes; however, these processes require parasitic loads. Recent developments in dual-phase mixed ionic/electronic conducting systems, particularly mixed oxide-ion/carbonate-ion conductors (MOCC) and mixed electronic/carbonate-ion conductors (MECC), have made these conductors promising CO_2 separation/capture choices. These materials initially developed as electrolyte materials for fuel cells utilizing fossil fuels are ideal for separating CO_2 from flue gas (MECC) or a reducing stream (MOCC). These processes prove to be advantageous due to not requiring any steam or chemical load in order to drive the CO and CO_2 shifting reaction.

A popular method for synthesizing these membranes is through creating porous matrix and then infiltrating the matrix with a molten carbonate (MC). MOCC is ideal for separation during a reducing stream comprised of $CO_2 + H_2O$; in this case, CO_3^{2-} and O^{2-} act as electrochemical gradients in opposite directions across the membrane, allowing for the separation process to occur. In the case of MECC, separation is ideal for oxidizing streams of flue gas. The electrochemical gradient in MECC separation membranes are

CO_3^{2-} and e^- . During the separation process, the MC within the matrix has a tendency to leave the porous matrix. The matrix can be infiltrated again and reused, an advantage of these CO_2 capture/separation systems. Both MOCC and MECC systems still require improvement during the operation due to potential loss of MC. One possible method of improving the retention of MC phase in the porous matrix is through the reduction of contact angle between MC and the matrix. Since Al_2O_3 is known to have a nearly zero contact angle with MC, it is then reasonable to incorporate a layer of Al_2O_3 on the outer surface of the matrix before MC is filled.

4.2 EXPERIMENTAL

To demonstrate the concept, a silver matrix was used as a model system. Firstly, the silver skeletal matrix was created through mixing 1-3μm Ag powder with carbon black. This powder was then pressed into 25mm diameter pellets before being fired at 650°C for 2 hours. The firing process would burn out the carbon, leaving behind a porous silver matrix.

The studies focus revolves around an added a layer of an Al_2O_3 coating to the porous matrix before molten carbonate (MC) infiltration. The presence of Al_2O_3 layer can improve the adhesion of MC to the skeletal by reducing the contact angle, which ultimately increases the retention of MC during high temperature operation. To incorporate such a layer of Al_2O_3 on the surface of porous matrix, the silver matrix was first vacuum sealed to remove air from the pores before infiltrating. The concentration of Al_2O_3 colloidal was 20%. The sample was then removed from the vacuum and fired to 400°C for 2 hours to remove liquid from the sample. This process of infiltration and firing was repeated once for one sample and repeated three more times for another in order to compare the thickness of the aluminum layers. These samples were analyzed using a Zeiss Ultra Plus scanning electron microscope (SEM).

For further studies, a 62:38 mol% Li_2CO_3+K_2CO_3 MC was prepared for infiltrating the porous matrix. The porous samples were suspended by a silver wire and slowly submerged in the MC at a temperature of 700°C. During the cooling process, the sample was removed from the MC at a temperature of 500°C, a temperature slightly higher than the solidification temperature of the MC. These fabricated samples also underwent SEM analysis.

The MECC membrane was sealed in between two alumina tubings using a sealant comprised of ceramic cement and a commercial glass powder [35]. The assembly was cured at 93°C for 4 hours. A flue gas (CO_2-O_2 1:1 molar mixture) was delivered at a flow rate of 100 mL/minute, along with N_2 tracer gas at 20 mL/minute for leak detection, to the targeted end of the MECC membrane [35]. High purity helium was utilized as a sweeping gas, with a flow rate of 50 mL/minute, being delivered to the permeate side of the sample. All flow rate were controlled using Smart-Trak 50 Series mass flow controllers. Analysis was conducted at a temperature range of 500°C to 650°C. Using a Varian 490 micro GC, the CO_2 concentration could then be measured on the separation end of the MECC membrane. Figure 4.1 gives a detailed diagram of the experimental set up [15].

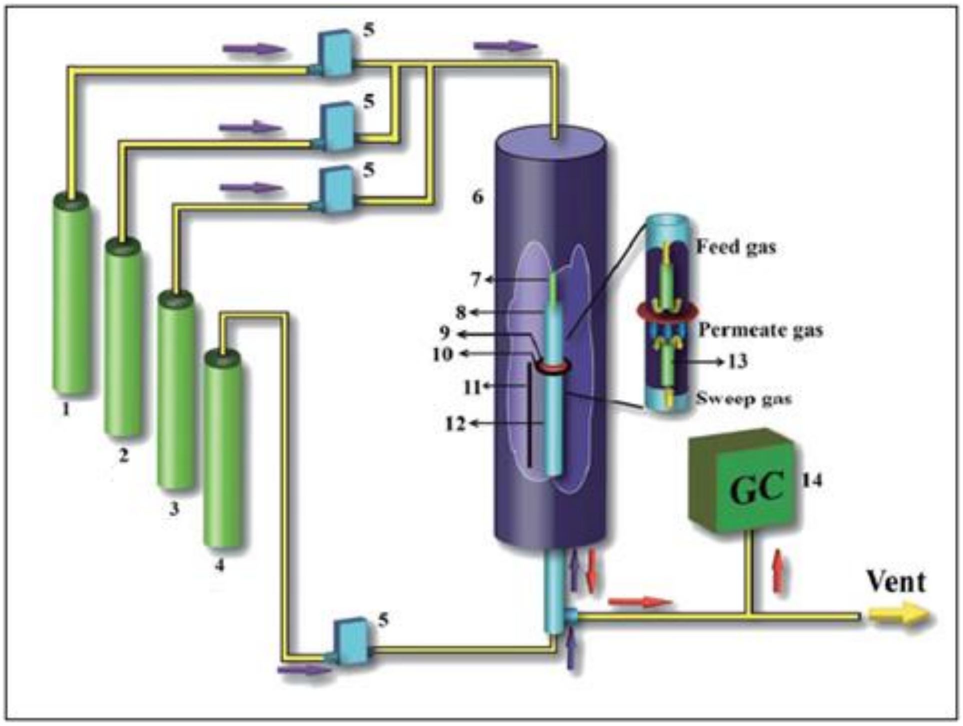

Figure 4.1 “Schematic of the CO_2 permeation cell configurations. (1) CO_2 cylinder; (2) nitrogen cylinder; (3) oxygen cylinder; (4) helium cylinder; (5) mass flow controllers; (6) furnace; (7) inner feed tube; (8) second short alumina tube; (9) MOCC membrane; (10) sealant; (11) thermocouple; (12) supporting alumina tube; (13) inner sweep tube; and (14) gas chromatography.” [15]

Equations 4.1 through 4.3 were used for calculating the flux densities of CO_2, O_2, and N_2 [35]. The measured concentrations of CO_2 (total), O_2 (total), and N_2 (leakage) are denoted by C_{CO2}, C_{O2}, and C_{N2} respectively; Q is the flow rate of the He sweeping gas; and the effective reaction are of the sample is denoted by S [35]. Final fluxes of CO_2 and O_2 were corrected for N_2 leakage using equations 4.4 and 4.5; the ratio between flow rates of CO_2 and N_2 serves as the correction coefficient of 2.5 [35].

$$J_{N2} = \frac{C_{N2}}{(1-C_{CO2}-C_{O2}-C_{N2})} \times \frac{Q}{S} \tag{4.1}$$

$$J_{CO2(total)} = \frac{C_{CO2}}{(1 - C_{CO2} - C_{O2} - C_{N2})} \times \frac{Q}{S} \quad (4.2)$$

$$J_{O2(total)} = \frac{C_{O2}}{(1 - C_{CO2} - C_{O2} - C_{N2})} \times \frac{Q}{S} \quad (4.3)$$

$$J_{CO2} = J_{CO2(total)} - 2.5 \times J_{N2} \quad (4.4)$$

$$J_{O2} = J_{O2(total)} - 2.5 \times J_{N2} \quad (4.5)$$

4.3 RESULTS AND DISCUSSION

The silver matrices coated with a layer of Al_2O_3, through the Al_2O_3 infiltration process previously discussed, were fractured and observed with SEM. Figure 4.2 compares an Ag matrix infiltrated twice versus an Ag matrix infiltrated four times under a 500x magnification using secondary electrons for detection. It appears that the pore size for both sample types is extensively smaller when compared with an Ag matrix without an Al_2O_3 layer.

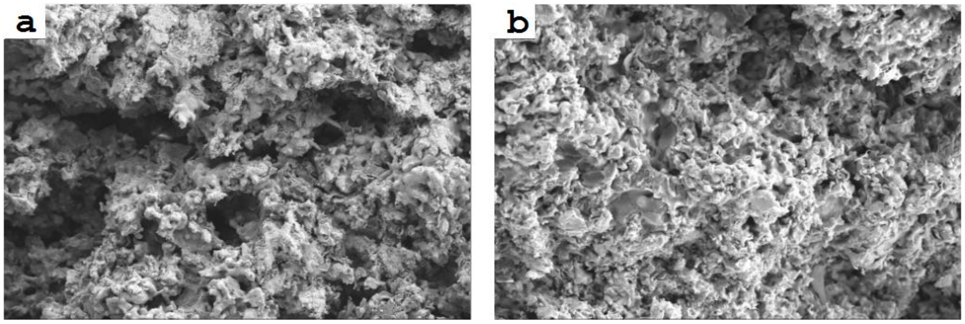

Figure 4.2 Microstructures of Ag matrix; a) Ag matrix infiltrated 2x, b) Ag matrix infiltrated 4x at 500x magnification detecting secondary electrons

Figure 4.3 compares the same two Ag matrices using both secondary and backscattering electrons. These images were taken 2000x magnification. Focusing on the backscatter data, the lighter portions of the material is attributed to Ag in the sample, while the darker portions are more representative of the Al content. The Ag samples infiltrated four times have a noticeably larger Al content. Due to the reduced pore size in these samples, new Ag matrices were infiltrated using diluted concentrations of Al_2O_3 to prevent this reduction.

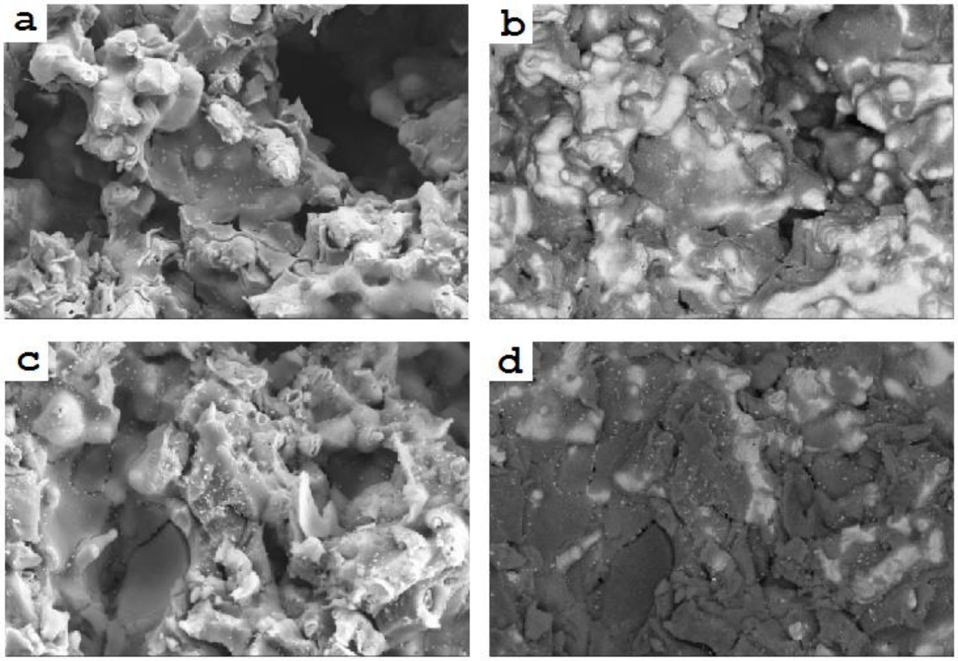

Figure 4.3 Microstructures of Ag matrix; a)Ag matrix infiltrated 2x under SE detection, b) Ag matrix infiltrated 2x under BSE detection, c) Ag matrix infiltrated 4x under SE detection, d) Ag matrix infiltrated 4x under BSE detection

A silver matrix was prepared by infiltrating a diluted amount of Al_2O_3, 10%, twice. The silver matrix prepared with an Al_2O_3 layer was infiltrated with MC, Li_2CO_3 and K_2CO_3 62:38 mol%. The sample was photographed with SEM, Figure 4.4. This sample also underwent gas chromatography analysis and was plotted against data from another MECC prepared without the additional Al_2O_3 layer, Figure 4.5. Gas chromatography was conducted with a homemade permeation cell system. From Figure 4.5, a distinct increase in the flux density was observed, especially at higher temperatures, suggesting that increasing the retention of molten carbonate can indeed improve CO_2 flux density.

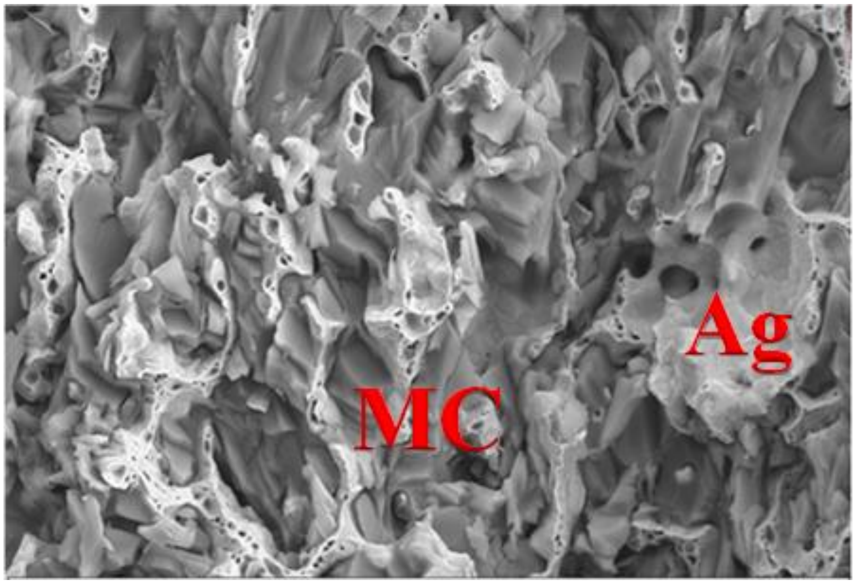

Figure 4.4 Microstructure of Ag matrix infiltrated with MC at 2000x magnification.

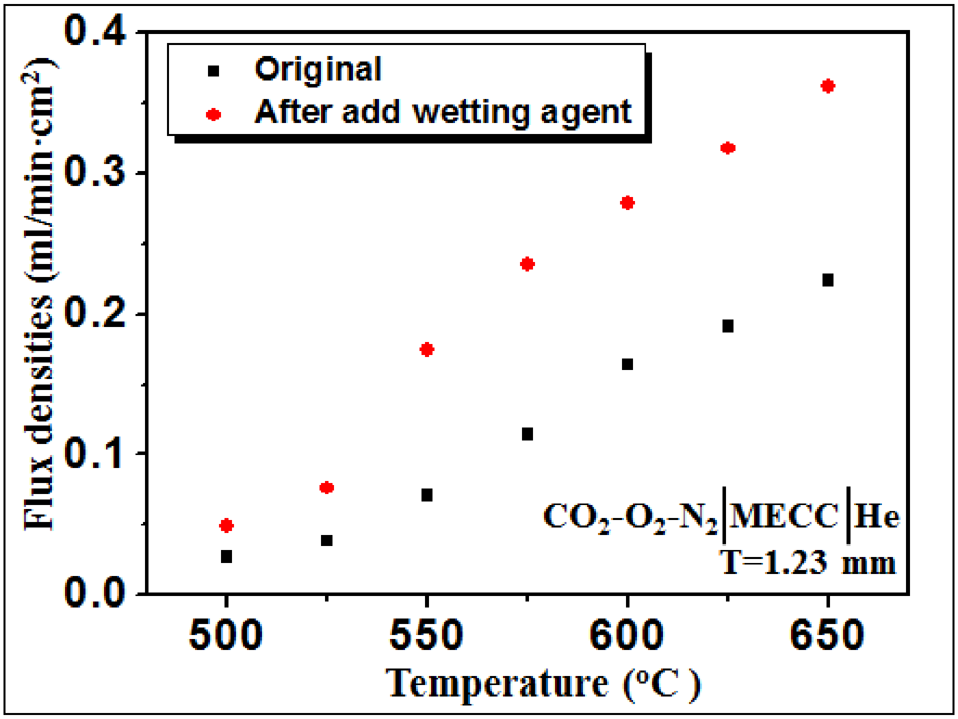

Figure 4.5 CO_2 flux density of MECC membranes with and without an additional Al_2O_3 layer measured as a function of temperature.

CHAPTER 5:

CONCLUSIONS

Yttrium-doped barium zirconate, particularly $BaZr_{0.8}Y_{0.2}O_{3-\delta}$, has garnered a great deal of attention due to its incredible proton conductivity, its ability to withstand acidic atmospheres, and small activation energy requirement. Unfortunately this promising electrolyte suffers from poor conductivity at the grain boundaries and its difficulty with densification during the sintering process. With regards to densification, BZY requires high sintering temperatures for long time intervals; wet chemical synthesis has since become a common method for partially reducing these sintering temperatures. Using a new sintering method to induce a transient liquid phase within the studied material, it may be possible to reduce sintering temperatures without the use of complicated wet chemical synthesis, or significantly affecting the mechanical strength of the material. To determine whether the transient liquid phase sintering method can be utilized as a potential method for electrolyte synthesis, the chosen material, BZY20, was characterized using a number of common testing methods.

The transient liquid-phase sintering method has proven to be a viable option for sintering electrolyte materials. Focusing on the proton conducting yttrium-doped (20mol%) barium zirconate (BZY20) and, $BaO:Ga_2O_3$ 68:32 Mol% barium gallate (BG) was chosen as a flux to aid densification during the sintering process. By using this new method for densification, sintering temperatures can be lowered to 1300°C for 10 hours.

TMA shows that the bulk of the sintering process is completed within the first 4 hours. Due to this fact, the sintering process may possibly be reduced from the 10 hour holding time to a shorter period of time. Based on data gathered using the Archimedes principle and SEM analysis, it is evident that densification is dependent on the BG content used during sintering. Using a larger BG content will yield a denser material. However, from EIS analysis it is also evident that a higher BG content will yield lower conductivity and higher activation energy. During EIS analyses, different atmospheric conditions introduced various amounts of humidity to see how conductivity is affected. The gathered data suggests that higher humidity's will yield higher conductivities, at least to a point. Although being a proton conductor, a humidity of 10.51% H_2O displayed a slightly lower conductivity than an atmosphere containing 5.57% pH_2O.

In a paper by E. Fabbri in 2010, BZY with various molar percentages of yttrium were characterized. An observation was made stating that doping barium zirconate with a yttrium content higher than 20mol% was not beneficial for proton conductivity. This was partially due to a loss in barium with higher amounts of yttrium, which in turn causes consequential formations that block proton migration [26]. A possible future study may focus on observing conductivity in BZY samples doping with higher yttrium contents that are synthesized with larger BG contents.

A new family of oxide-ion conductors, $Sr_{1-x}K_xSi_{1-y}Ge_yO_{3-0.5x}$, was recently reported by Preetam Singh and John Goodenough. In an attempt to further study and explore new possibilities with this new oxide-ion conductor, the germanium component of the material was replaced with gallium. Gallium based oxides are known to promote fast ion conduction; with this in mind $Sr_{1-x}K_xSi_{1-y}Ga_yO_{3-0.5x}$ was characterized as a potential oxide-ion conducting electrolyte material.

The data gathered through EIS suggests that $Sr_{1-x}K_xSi_{1-y}Ga_yO_{3-0.5x}$ has a lower conductivity than the $Sr_{1-x}K_xSi_{1-y}Ge_yO_{3-0.5x}$ system investigated by Singh. Through both XRD analysis and SEM photographs, there appears to be a noticeable change in $Sr_{0.8}K_{0.2}Si_{1-y}Ga_yO_{3-0.5x}$ (y = 0.2 and 0.3). For the two compositions stated, the intensity of peaks in the diffractogram change when compared with the baseline, $Sr_{0.8}K_{0.2}Si_{0.5}Ge_{0.5}O_{3-\delta}$, and $Sr_{0.8}K_{0.2}Si_{0.9}Ga_{0.1}O_{3-\delta}$. The SEM photographs for $Sr_{0.8}K_{0.2}Si_{1-y}Ga_yO_{3-0.5x}$ (y = 0.2 and 0.3) show crystal formations within the pores of the material and there is a noticeably large amount of charge in the photographs; this observation was not seen during the analysis of the other samples.

Future studies on characterizing $Sr_{1-x}K_xSi_{1-y}Ge_yO_{3-0.5x}$ may wish to focus on the substitution of germanium with gallium. Gallium is widely considered to be influential to both proton and oxide-ion conductivity in ion conducting materials. The work of P. Singh and J. Goodenough characterizes a wide variety of materials in the newly discovered $Sr_{1-x}K_xSi_{1-y}Ge_yO_{3-0.5x}$ family. In Singh's study, $Sr_{1-x}K_xMO_{3-0.5}$ (M = Si or Ge) serves as a basic template for the material of interest; it is possible to improve oxide-ion conductivity at smaller amounts of Ga than previously studied (y < 0.1).

CO_2 separation and capture systems are being considered as the quickest method for returning carbon balance to the ecosystem and reducing environmentally harmful emissions from fossil fuel based power plants. Recent developments in mixed oxide-ion/carbonate-ion conductors (MOCC) and mixed electron/carbonate-ion conductors (MECC) have garnered interest as CO_2 separation membranes. Focusing on MECC CO_2

capture systems, a skeletal silver matrix was coated with a layer of Al_2O_3 to aid the molten carbonate retention. The results clearly show that Al_2O_3 coating help the retention of molten carbonate and therefore increase the CO_2 permeation flux.

Adding an Al_2O_3 layer to a porous Ag matrix has a noticeable effect on the MC infiltration process for MECC samples. Future work should focus on further characterizing the Al_2O_3 layer's effect on MC infiltration and MECC performance. MC retention for MOCC systems may also benefit from a similar process of adding a thin layer of inert electrolyte support material to the porous matrix.

.

REFERENCES

[1] E. Fabbri, D. Pergolesi, E. Traversa, *Advanced Materials*, 24 (2012) 195

[2] S.P. Jiang, *Int. J. Hydrogen Energy*, 37 (2012) 449

[3] B. C. H Steele, A. Heinzel, *Nature*, 414 (2001) 345

[4] A. D. Epifanio, E. Fabbri, E. Di Bartolomeo, S. Licoccia, E. Traversa, *Fuel Cells*, 1 (2009) 69

[5] S. V. Bhide, A. V. Virkar, *J. Electrochem. Soc*,. 146 (1999) 2038

[6] N. Zakowsky, S. Williamson, J. T. S. Irvine, *Solid State Ionics*, 176 (2007) 3019

[7] S. B. C Duval, P. Holtappels, U. Stimming, T. Graule, *Solid State Ionics*, 179 (2008) 1112

[8] J. Tong, D. Clark, M. Hoban, R. O'Hayre, *Solid State Ionics*, 181 (2010) 496

[9] T. Norby, N. Christiansen, *Solid State Ionics*, 77 (1995) 240

[10] K. Amezawa, H. Maekawa, Y. Tomii, N. Yamamoto, *Solid State Ionics*, 145 (2001) 233

[11] S. Li, F. Schonberger, P. Slater, *Chem. Commun.*, (2003) 2694

[12] L. Chick, J. Liu, J. Stevenson, T. Armstrong, D. McCready, G. Maupin, G. Coffey, C. Coyle, *J. Am. Ceram. Soc.*, 80 (1997) 2109

[13] U.S. Energy Information Administration, *Energy Perspective 1949-2010*, 19 Oct. 2011

[14] U.S. Energy Information Administration, *Annual Energy Outlook 2011*, 26 April 2011

[15] L. Zhang, N. Xu, X. Li, S. Wang, K. Huang, W. Harris, W. Chiu, *Energy Environ. Sci.*, 5 (2012) 8310

[16] DOE/NETL, *Carbon Dioxide Capture R&D Program: Technology Update*, Sept. 2010

[17] E. Favre, *J. Membr. Sci.*, 294 (2005) 50

[18] S. Sherman, K. Brinkman, J. Gray, K. Huang, *J. Membr. Sci.*, 401-402 (2012) 323

[19] ARPA-E Carbon Capture Programs, *Taillores Post-Combustion Carbon Capture Workshop*, 11 July 2010

[20] C. F. Hendricks, *Energy Eviron.*, 1 (1994) 19

[21] X. Li, N. Xu, L. Zhang, K. Huang, *Electrochem Comm.*, 13 (2011) 694

[22] I. Hideaki, T. Hiroaki, *Solid State Ionics*, 86 (1996) 1

[23] T. Ishihara, H. Matsuda, Y. Takita, *J. Am. Chem. Soc.*, 116 (1994) 3801

[24] M. Feng, J. B. Goodenough, *Eur. J. Solid State Inorg. Chem.*, 31 (1994) 663

[24] P. Singh, J. B. Goodenough, *Energy Environ Sci.*, 5 (2012) 9626

[25] E. Kendrick, J. Kendrick, K. S. Knight, M. S. Islam, P. R. Slater, *Nature Mater.*, 6 (2007) 871

[26] E. Fabbri, D. Pergolesi, S. Licoccia, E. Traversa, *Solid State Ionics*, 181 (2010) 1043

[27] Y. Yamazaki, R. Hernandez-Sanchez, S. M. Haile, *Chem. Mater.*, 21 (2009) 2755

[28] A. Magrez, T. Schober, *Solid State Ionics*, 175 (2004) 585

[29] S. B. C. Duval, P. Holtappels, U. F. Vogt, E. Pomjakushina, K. Conder, U. Stimming, T. Graule, *Solid State Ionics*, 178 (2007) 1437

[30] K. Huang, R. S. Tichy, J. B. Goodenough, *J. Am. Ceram. Soc.*, 81 (1998) 2565

[31] S. M. Haile, G. Staneff, K. H. Ryu, *J. of Mater. Sci.*, 36 (2001) 1149

[32] T. Shimura, S. Fujimoto, H. Iwahara, *Solid State Ionics*, 143 (2001) 117

[33] L. Zhang, X. Li, S. Wang, K. G. Romito, K. Huang, *Electrochem. Comm.*, 13 (2011) 554

[34] X. Li, G. Xiao, K. Huang, *J. of Electrochem. Soc.*, 158 (2011) B225

[35] N. Xu, L. Zhang, X. Li, M. Franks, J. Thomason, K. Huang, *The Electrochem. Soc.*, 45 (2012) 87

[36] N. Xu, X. Li, M. Franks, H. Zhao, K. Huang, *J. of Membr. Sci.*, 401-402 (2012) 190

[37] K. D. Kreuer, S. Adams, W. Munch, A. Fuchs, U. Klock, J. Maier, *Solid State Ionics*, 145 (2001) 295

[38] K. D. Kreuer, *Solid State Ionics*, 125 (1999) 285

[39] H. G. Bohn, T. Schober, *J. Am. Ceram. Soc.*, 83 (2000) 768

[40] S. De Souza, S.J. Visco, L. C. De Jonghe, *Solid State Ionics*, 98 (1997) 57

[41] H. Iwahara, T. Yajima, T. Hibino, K. Ozaki, H. Suzuki, *Solid State Ionics*, 61 (1993) 65

[42] P. Babilo, S. M. Haile, *J. Am Ceram. Soc.*, 88 (2005) 2362

[43] P. Babilo, T. Uda, S. M. Haile, *J. Mater. Res.*, 22 (2007) 1322

[44] F. Iguchi, T. Yamda, N. Sata, T. Tsurui, H. Yugami, *Solid State Ionics*, 177 (2006) 2381

[45] J. B. Goodenough, *Nature*, 404 (2000) 821

[46] X. D. Wang, Y. Ma, R. Raza, M. Muhammed, B. Zhu, *Electrochem. Commun.*, 10 (2008) 1617

[47] R. Bredesen, K. Jordal, O. Bolland, *Chem. Eng. Process.*, 43 (2004) 1129

[48] B. J. P Buhre, L. K. Elliott, C. D. Sheng, R. P. Cupta, T. F. Wall, *Prog. Ener. Comb. Sci.*, 31 (2005) 283

[49] D. Shekhawal, D. R. Luebke, H. W. Pennline, DOE/NETL, 2003

[50] H. Kawamura, et al., *J. Chem. Eng. Jpn.*, 38 (2005) 322

[51] E. J. Granite, T. O'Brien, *Fuel Processing Technol*, 86 (2005) 1423

[52] S. J. Chung, J. H. Park, D. Li, J. I. Ida, I. Kumakiri, Y. S. Lin, *Ind. Eng. Chem. Res.*, 44 (2005) 7999

[53] K. S. Lackner, A. C. West, J. L. Wade, U. Columbia (Ed.), WO2006113674, United States, 2006

[54] M. Anderson, Y. S. Lin, *J. Membr. Sci.*, 357 (2010) 122

[55] J. Wade, C. Lee, A. C. West, K. S. Lackner, *J. Membr. Sci.*, 369 (2011) 20